J. Fluid Mech. (2007), *vol.* 579, *pp.* 227–270.
doi:10.1017/S0022112007004971 Printed in the United Kingdom

Direct numerical simulation of turbulent Taylor–Couette flow

M. BILSON AND K. BREMHORST

Division of Mechanical Engineering, The University of Queensland, Brisbane, 4072, Australia

(Received 29 August 2005 and in revised form 19 November 2006)

Direct numerical simulation (DNS) is used to investigate turbulent Taylor–Couette (TC) flow. A simulation was run for a Reynolds number of 3200 in an apparatus with a radius ratio of $\eta = 0.617$ and an aspect ratio of 4.58, which assumed a vortex pair wavelength of 2.29. Results reported include the mean velocity, velocity fluctuation intensities, Reynolds stress budgets, and visualizations of the instantaneous velocity fluctuation field. Secondary near-wall vortex pairs are observed near to the cylinder in addition to the Taylor vortex (TV) motion. Weaker evidence of secondary vortices is found at the outer cylinder where a banded structure has been identified. The azimuthal wall shear stress component shows large peaks and valleys at stagnation points on the surface of both cylinders where flow from neighbouring vortices impacts on the respective wall. These stagnation points correspond to locations where the secondary vortices have been identified. The effect of the mean TV motion is reflected in the Reynolds stress budgets which are similar to but more complex than those of two-dimensional boundary layers. Visualization of the turbulent velocity fluctuations reveals near-wall streaks at the inner cylinder.

1. Introduction

Laminar and turbulent flow in the Taylor–Couette (TC) apparatus are of interest for many practical and theoretical purposes. The apparatus consists of two concentric cylinders, where the rotation of one or both of the cylinders results in fluid motion. In this paper, rotation of the inner cylinder alone is considered. Significant interest in TC flow first arose when an initial transition from laminar Couette flow to a laminar flow state that consists of pairs of counter-rotating vortices was predicted mathematically and verified experimentally (Taylor 1923). This motion is commonly referred to as a Taylor vortex (TV) motion. When the rotation rate of the inner cylinder is increased further, even more laminar flow states are identified. Many of these laminar flow states, or at least their initial transition, can be predicted theoretically. For this reason, laminar TC flow has attracted wide interest (Tagg 1994).

From a practical perspective, the TC apparatus is a good representation of several devices. Examples include, rotating machinery such as journal bearings, rotating cylinders for corrosion research (Gabe 1974; Gabe & Walsh 1983; Gabe *et al.* 1998), viscosity measurement devices, and biological applications (Haut *et al.* 2003). The fluid flow is generally turbulent in these applications. A characteristic of turbulent flow in the TC apparatus is the presence of a mean TV motion that is very similar to the TV motion for laminar flow. In turbulent flow, however, the vortex boundaries and the flow generally are irregular in an instantaneous sense. However, the mean TV motion does remain stationary in the axial direction. Visual evidence of a TV motion

in turbulent TC flow has been reported in several studies (Coles 1965; Fenstermacher, Swinney & Gollub 1979; Andereck, Liu & Swinney 1986; Parker & Merati 1996). The TV motion is present just beyond the onset of turbulence and it typically remains visible up to very large Reynolds numbers. However, as the Reynolds number is increased, the small-scale motion becomes more dominant until eventually the visual structure of the vortex motion is diffused by the increasing turbulence intensity (Barcilon & Brindley 1984).

Despite the practical significance of turbulent TC flow, only a small number of experimental and numerical investigations have been carried out. There are relatively few quantitative investigations of turbulence statistics and the effect of the TC motion on these results. Also, visualization studies have been hampered by the curved surfaces of the device causing light to be refracted. We review previous work, and then analyse the results from a direct numerical simulation (DNS) of turbulent TC flow. With DNS, the governing equations of fluid motion are solved with a grid and time step small enough to resolve turbulent motion down to the dissipative length scales. It is an ideal technique for the present study because turbulence models are not required, and therefore it provides an accurate description of the physics contained in the Navier–Stokes equations (Moin & Mahesh 1998). Our results will lead to a greater understanding of turbulent TC flow and the effects of the TV motion, which will contribute to an improved understanding of the function of engineering applications of TC flow devices.

2. Previous work

While TC flow cases with both cylinders rotating are of interest, the present review and work are restricted to a case where only the inner cylinder rotates. Other reviews should be referred to for an account of cases with both cylinders rotating (e.g. Andereck *et al.* 1986).

The geometric parameters of the TC apparatus (figure 1) are the ratio of inner to outer cylinder radius η,

$$\eta = \frac{R_1}{R_2}, \tag{2.1}$$

and the ratio of cylinder length (L_x) to gap width between the cylinders (aspect ratio Γ),

$$\Gamma = \frac{L_x}{(R_2 - R_1)}. \tag{2.2}$$

TC flow is characterized by the geometric parameters of the device, the tangential velocity of the inner cylinder (W_1) and the kinematic viscosity (ν). These parameters are combined to form dimensionless groups that characterize the flow, namely the Reynolds number Re_1,

$$Re_1 = \frac{W_1(R_2 - R_1)}{\nu}, \tag{2.3}$$

and the Taylor number Ta,

$$Ta_1 = 4Re_1^2 \left(\frac{1-\eta}{1+\eta}\right). \tag{2.4}$$

The definitions of Reynolds and Taylor numbers vary in the literature and the definitions given in (2.3) and (2.4) reflect what is used in the present work. The

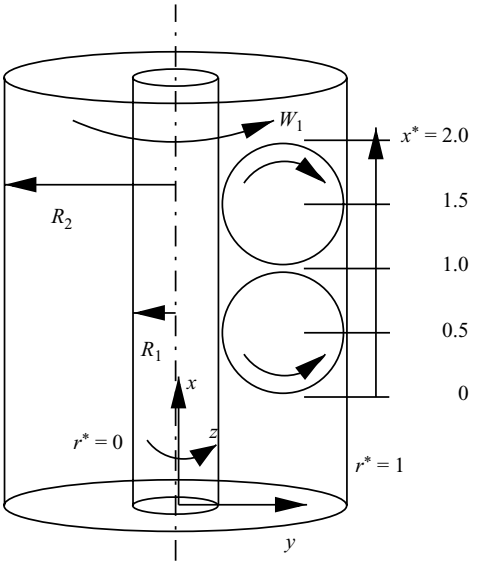

FIGURE 1. The TC configuration.

Reynolds and Taylor numbers are similar quantities; however, the Taylor number accounts for differences in the radius ratio.

The onset of turbulent motion in the TC apparatus is a function of the Reynolds (Taylor) number, the radius ratio, aspect ratio, and even the starting laminar flow condition. In studies that have investigated the transition to turbulence, a range of Reynolds numbers has been reported for the onset of turbulent flow. For example, Andereck *et al.* (1986) report turbulent flow at $Re_1 = 2890\,(\eta = 0.908)$, Smith & Townsend (1982) report turbulence at $Re_1 = 7300\,(\eta = 0.667)$ and Koschmieder (1979) at $Re_1 = 1290\,(\eta = 0.727)$. Hence, it is concluded that there is no unique Reynolds number for the onset of turbulent flow. However, it can be stated that once the Reynolds number is of the order of 1000 or more, transition to turbulent flow generally occurs.

Some of the first studies (Wattendorf 1935; Taylor 1935) of turbulent TV motion reported measurements (using Pitot tubes) of the azimuthal velocity component, but they did not account for the TV motion as the results were averaged along the cylinder axis. Smith & Townsend (1982) used hot-wire anemometers (HWA) to measure azimuthal, axial and radial velocity components. They introduced a small axial velocity to move the vortices past the measuring location and thus isolate the influence of the TV motion on the velocity output. The resulting measured velocity was phase-averaged to measure the relative contribution of the TV motion to the velocity fluctuation. It was shown that the relative contribution of the TV motion to the velocity fluctuation decreased with increasing Reynolds number. This work, however, relied on the assumption that the TV motion was completely separated from turbulent motions in a spectral sense (that is, there were no low-frequency turbulent velocity fluctuations). The axial variation of the TV motion and velocity fluctuations was not reported.

Wereley & Lueptow (1994) made velocity measurements that directly include and report the axial dependence of velocity components and hence provide information on the influence of the TV motion. Azimuthal component velocity profiles, measured with a laser-Doppler velocimeter, were reported and the TV motion was found to

have the greatest effect on the mean azimuthal velocity away from the cylinder walls, where the azimuthal velocity changed significantly in the direction of the cylinder axis. Radial and axial velocity component measurements made using HWA at varying axial locations have also been reported (Kobayashi *et al.* 1990), as have similar measurements using laser-Doppler anemometers (LDA) (Parker & Merati 1996). For both experiments, the time-averaged velocity and turbulence measurements were found to change significantly, depending on the axial location relative to the TV. Visual evidence of the TV motion has been reported at a Reynolds number of 73 000 (Parker & Merati 1996), a magnitude well beyond that typically observed for the initial transition to turbulence. Based on this, the axial dependence of turbulence statistics cannot be discounted as an isolated feature for lower-Reynolds-number turbulent TC flow.

Small-scale motion within the TV has been studied using visual techniques at the outer cylinder, and a motion similar to a Görtler vortex (GV) has been identified (Barcilon & Brindley 1984). The GV motion is believed to occur as a result of curved surfaces and it consists of pairs of counter-rotating vortices having their axes oriented in the streamwise direction. In TC flow, the GV occurs at a length scale much smaller than the TV, and it is restricted to the near-wall region. Increases of the Reynolds number in this particular study led to the size of the GV decreasing; however, at Reynolds numbers where the TV was not visible the GV motion could still be seen. The authors concluded that turbulent TC flow is composed of two forms of coherent motion: the TV and the GV.

Our review thus far has been restricted to experimental work. Measurements of velocity and hence reporting of turbulence statistics in turbulent TC flow have been restricted in the past because the closed system means that probes can cause significant interference which feeds back to the incoming flow. The cylindrical shape has made some visual measurement techniques difficult as a result of refraction. We have used numerical techniques here as they do not suffer from these limitations.

Turbulent flow contains length scales spanning over several orders of magnitude and as a result DNS is computationally expensive; however, the technique's accuracy makes it ideal for computation of turbulence statistics that otherwise cannot be measured. Only a small number of DNS studies of turbulent TC flow have been reported. Yuu & Umekage (1995) ran a simulation for a case with $Re_1 = 1500$, $\Gamma = 20$, and $\eta = 0.88$. They produced a DNS that agreed well with the experiments that they ran in parallel. This work showed the significant cylinder end effects on the velocity field when in the vicinity of the cylinder ends.

DNS of turbulent flow for a case with the inner and outer cylinders rotating has been reported (Rudman & Blackburn 1998); the Reynolds number was 3000, based on the difference in velocity between the two cylinders. Radius ratios of $\eta = 0.875$ and $\eta = 0.667$ were tested. The flow state corresponded to featureless turbulence and hence no considerations of the influence of TV motion were reported. Rudman & Blackburn presented contour plots of instantaneous velocity and observed a very streaky flow structure near the inner cylinder and a somewhat less streaky flow structure toward the outer cylinder. Mean velocity profiles showed that a laminar sublayer existed (that is, $u^+ = y^+$) near the wall ($y^+ < 10$), and away from the wall the profile followed logarithmic laws.

Turbulent TC flow has been considered extensively with Reynolds-averaged Navier–Stokes (RANS) turbulence modelling methods because of their reduced computational expense. A major shortcoming of RANS models is that the turbulence is modelled rather than directly computed. A selection of previous work is discussed below to illustrate the versatility of this approach.

The influence of the radius ratio on the mean TV motion was considered for a case with a Reynolds number of $Re_1 = 50\,000$ (Kobayashi, Matsubara & Maekawa 1999). The k–ϵ turbulence model was applied. It was found that the vorticity of the TV motion was greatest for $\eta = 0.7$ and that it decreased rapidly for lower values of η, thus suggesting that both cylinders play an important role in maintaining the TV motion in turbulent TC flow.

The k–ω turbulence model was used to investigate transitions for higher-Reynolds-number turbulent TC flow (Batten, Bressloff & Turnock 2002). Radius ratios of $\eta = 0.734$, 0.941 and 0.985 were tested for Reynolds numbers ranging from $Re_1 = 5000$ to $Re_1 = 20\,000$. The work identified a secondary transition in the turbulent flow state similar to that observed in experiments (Lathrop, Fineberg & Swinney 1992). Batten *et al.* (2002) also found that the secondary transition occurred at lower Reynolds numbers for increasing gap width. Whilst this work was limited by the applicability of RANS models, it demonstrated the potential of simulation to extend TC studies into regions where experimental work cannot economically reach.

RANS turbulence modelling has also been used to investigate end effects for finite-length cylinders. Wild, Djilali & Vickers (1996) investigated the contribution of the cylinder ends to the total torque. The cylinder aspect ratio was varied from $\Gamma = 2$ to $\Gamma = 40$ and the Reynolds number from $Re_1 = 3000$ to $Re_1 = 40\,000$. Several turbulence models were used and it was found that for smaller aspect ratios, the contribution to the total torque from the disks at the end of each cylinder represented a substantial fraction of the total torque. At smaller aspect ratios it was also found that the torque variation along the cylinder axis was more significant than it was for the larger aspect ratios. This work was particularly valuable because it allowed a wide range of parameters to be varied and their effect on a widely used and experimentally measured quantity to be determined.

A great deal of qualitative and quantitative information is known about turbulent TC flow. The TV motion persists up to very high Reynolds numbers and few studies consider the disappearance of the TV motion. Several studies consider measurements of the mean velocity and turbulent velocity fluctuations at varying locations within the TV. However, there is relatively little quantitative investigation of turbulence statistics or visualization of the turbulent flow and discussion of the subsequent influence of the mean TV motion, and this is a topic for further investigation in this paper.

3. Numerical method

The fluid was assumed to be incompressible and Newtonian. The governing equations for fluid motion under these assumptions are the continuity equation,

$$\nabla \cdot \boldsymbol{u} = 0, \tag{3.1}$$

and the Navier–Stokes equation,

$$\frac{\partial \boldsymbol{u}}{\partial t} = -\nabla p + \frac{1}{Re_1}\nabla \cdot \nabla \boldsymbol{u} - \nabla \cdot (\boldsymbol{u}\boldsymbol{u}), \tag{3.2}$$

where $\boldsymbol{u}$ is the velocity vector and p is the pressure. The equations are normalized by the gap width between the cylinders ($R_2 - R_1$), and the tangential velocity of the inner cylinder W_1. Time is normalized by the characteristic length and velocity ($(R_2 - R_1)/W_1$), and the pressure term is normalized by the square of the characteristic velocity and density (ρW_1^2). The Reynolds number is defined according to (2.3).

The equations were discretized in space using a second-order-accurate finite-volume method (Ferziger & Peric 2002) on a staggered grid (Harlow & Welch 1965). The grid was based on a cylindrical coordinate system with an inertial reference frame since this is well-suited to the TC configuration (throughout this paper: $x =$ axial or spanwise coordinate; $u =$ axial or spanwise velocity; $y =$ radial or wall-normal coordinate; $v =$ radial or wall-normal velocity; $z =$ azimuthal or streamwise coordinate measured in radians; and $w =$ azimuthal or streamwise velocity). The grid was uniform in the axial and azimuthal directions, and refined near each cylinder surface using smooth transformation functions (Hoffman 1982; Vasilyev 2000). The governing equations were advanced in time with a second-order Adams–Bashforth method for explicitly advanced terms and the Crank–Nicolson method for implicitly advanced terms. All terms in the equations were advanced explicitly in time except for the wall-normal diffusion terms, which had a detrimental effect on the maximum allowed time step for numerical stability, and hence these terms were advanced implicitly (Akselvoll & Moin 1996). Pressure correction in the Navier–Stokes equations was accomplished with a fractional step method (Dukowicz & Dvinsky 1992; Perot 1993). The Poisson equation for pressure correction was solved using Fourier transforms to decouple the periodic directions and a tri-diagonal solver was used to invert the resulting matrix (Hockney 1965).

Boundary conditions were periodic in the axial and azimuthal directions and no slip at the inner and outer cylinders. The tangential velocity was set to a constant magnitude at the inner cylinder and zero at the outer cylinder.

4. Computation details and verification

4.1. *Axial domain length and starting procedure*

Figure 1 shows the computational domain and coordinate axes. The axial domain length of the simulation is defined in terms of the aspect ratio Γ, defined in (2.2). The aspect ratio can also be defined as the dimensionless TV pair wavelength λ, multiplied by the number of vortex pairs N, such that $\Gamma = \lambda N$. This definition assumes that an even number of vortex pairs will fit into a given space. For a numerical simulation with periodic end boundary conditions, this is forced to occur by counter-rotation of the vortices. In a computation using no-slip end boundary conditions or an experiment, odd numbers of vortices can result. In practice, these end vortices are usually ignored when defining the wavelength (Koschmieder 1979).

The wavelength of the vortices in the present work was based on experimental results (Kataoka, Doi & Komai 1977). A vortex wavelength of $\lambda = 2.29$ was used and the domain was made long enough to accommodate two vortex pairs or four individual vortices (that is, $\Gamma = 4.58$). An axial domain length of $\Gamma = 20$ is typical for experimental work (Parker & Merati 1996) and a similar domain length would have been required for a computation with no-slip end boundary conditions. This domain size was computationally impractical for turbulent flow. Periodic boundary conditions were used in the axial direction to avoid the computational expense that would have been involved with no-slip boundary conditions. The radius ratio was set to $\eta = 0.617$ to correspond to the experimental results on which the vortex wavelength was based (Kataoka *et al.* 1977).

The periodic boundary condition requires an *a priori* specification of the TV wavelength. The TV wavelength in experiments is influenced by the aspect ratio, radius ratio and starting procedure (Koschmieder 1979). There was no reason to expect that a numerical solution would not display similar effects. A set of coarse grid runs was done to check the influence of the domain length and starting procedure.

Parameters[a,b] Γ, λ	Possible flow states and achieved flow state (in bold) N, λ	N, λ	N, λ
$\Gamma = 2\lambda$, $\lambda = 2.00$	**2, 2.00**[*]	3, 1.33	4, 1.00
$\Gamma = 2\lambda$, $\lambda = 2.29$	**2, 2.29**[*]	3, 1.53	4, 1.15
$\Gamma = 8\lambda$, $\lambda = 2.00$	7, 2.29	8, 2.00	**9, 1.78**[*]
$\Gamma = 8\lambda$, $\lambda = 2.29$	7, 2.62	8, 2.29	**9, 2.04**[*]

[a] Grid resolution for coarse grid cases:
$\Delta x \approx 0.042$(e.g. $\Gamma = 4.0$, $N_x = 96$), $\Delta y_{min} = 0.005$, $\Delta y_{max} = 0.039$ ($N_y = 48$), $\Delta z = 0.049$ ($N_z = 128$).
[b] Simulation parameters, imposed wavelength.
[*] Resulting simulation flow state.

TABLE 1. TV wavelengths for turbulent TC flow with different domain lengths and vortex wavelengths for coarse grid tests (all cases based on instantaneous acceleration of the inner cylinder to the desired Reynolds number).

A coarse grid was used because it was not computationally possible to run the required number of cases on a fine grid. Details of the finer grid and methods used to gather statistics are provided in §§4.2 and 4.4, and coarse grid details are provided in table 1. Values of the vortex wavelength were set to $\lambda = 2.00$ or 2.29. Different values of λ were used in some initial test cases; however, the influence of this on the matters being investigated was assumed to be secondary.

For the cases reported in table 1, a mean streamwise velocity profile based on constant angular momentum across the gap between the cylinders was imposed at the start of the simulation. This has been measured in previous experiments (Smith & Townsend 1982). Random velocity components were used for the other two directions, and the streamwise velocity profile was disturbed by random perturbations to numerically trip a turbulent flow state. The cylinder Reynolds number was set to the desired value from the beginning of the simulation. This procedure was used for all simulations unless stated otherwise.

The first test case involved running two domain lengths of 2λ and 8λ (with $\lambda = 2.00$ or $\lambda = 2.29$). The primary result considered here was the vortex wavelength, which was identified from visual inspection of the mean velocity field. Generally, the vortex wavelength was expected to be approximately equal to 2.00 or 2.29, depending on the value of λ used. This was the case when $\Gamma = 2\lambda$ was the computational domain length, but at larger domain lengths other flow states (as identified by a different vortex wavelength) were observed to form.

Starting procedure was also investigated. Simulation parameters and results are summarized in table 2. The results show no sensitivity to starting procedure for the shorter domain length (that is, $\Gamma = 2$), although there is a sensitivity as the domain length increases (that is, at $\Gamma = 8$).

The results of the these test cases show that longer domain length computations tend to allow different TV wavelengths to form. For the shorter domain lengths, a consistent flow condition was achieved and the shorter domain was therefore considered most appropriate for the present work, as the ability to achieve multiple flow states at the same Reynolds number was not a topic of the present investigation.

4.2. *Simulation and post-processing details*

As noted in the previous section, computations were started from random perturbations imposed on a mean velocity profile with constant angular momentum

Geometric parameters[a]			
$L = 2\lambda$, $\lambda = 2.00$	$L = 2\lambda$, $\lambda = 2.00$	$L = 2\lambda$, $\lambda = 2.00$	$L = 8\lambda$, $\lambda = 2.00$
Starting procedure details			
Sudden acceleration to $Re_1 = 6000$, then run until stationary and then suddenly decrease to $Re_1 =$ 3200 and run until stationary.	Run until a TV is established at $Re_1 =$ 100, then suddenly accelerate to $Re_1 =$ 3200, and then run until stationary.	Increment Re_1 to operating value, start with random initial conditions at $Re_1 =$ 100, then set Re_1 to gradually increasing values: $Re_1 = 400$, 800, 1600 and 3200, and run until stationary for each case.	Increment Re_1 to operating value, start with random initial conditions at $Re_1 =$ 100, then set Re_1 to gradually increasing values: $Re_1 = 400$, 800, 1600 and 3200, and run until stationary for each case.
Resulting TV wavelengths			
$\lambda = 2.0$ (achieved for present case and also for a sudden start at $Re_1 = 3200$), see table 1.	$\lambda = 2.0$ (achieved for present case and also for a sudden start at $Re_1 = 3200$), see table 1.	$\lambda = 2.0$ (achieved for present case and also for a sudden start at $Re_1 =$ 3200), see table 1.	$\lambda = 2.0$ (achieved for present case) and $\lambda = 1.78$ (sudden start) at $Re_1 =$ 3200, see table 1.

[a] Grid resolution for coarse grid cases:
$\Delta x \approx 0.042$ (e.g. $\Gamma = 4.0$, $N_x = 96$), $\Delta y_{min} = 0.005$, $\Delta y_{max} = 0.039$ ($N_y = 48$), $\Delta z = 0.049$($N_z = 128$).

TABLE 2. TV wavelengths for turbulent TC flow, starting procedure investigation with different domain lengths for coarse grid cases.

Reynolds number:	3200	Grid number:	$256 \times 128 \times 384$
Grid spacing:[a,b]	$\Delta x^+ = 3.66$	$\Delta y^+ =$ varies from 0.35 to 2.97:	$R_1 \Delta z^+ = 5.39$
Radius ratio:	$\eta = 0.617$	Aspect ratio:	$\Gamma = 2 \times 2.29$
R_1:	$R_1 = 1.611$	R_2:	$R_2 = 2.611$
Vortex wavelength:	$\lambda = 2.29$	Number of samples:	72
Computational volume:	$\Gamma \times (R_2 - R_1) \times 2\pi$	Time between samples, t_m:	10[c]
Time step size:	0.005		

[a] Grid spacing in wall units based on τ_{yz_1}, where $\tau_{yz_1} = (1/Re_1)(\partial\langle w\rangle/\partial y - \langle w\rangle$ solidus $R_1)_1$, see § 4.2 for more information.
[b] Wall units are defined in the text.
[c] The value of t_m was estimated as the time for a large eddy to travel around the inner cylinder, $(2\pi R_1/W_1)(W_1/(R_2 - R_1)) = 10.1$.

TABLE 3. Computation details.

and were run until a stationary state was achieved. Other simulation parameters for the DNS are presented in table 3. Justification for these parameters is discussed in the following sections.

Statistics (mean velocity and other turbulence statistics) were computed by averaging an instantaneous three-dimensional solution over the azimuthal direction (averaged quantity denoted by $\langle\cdot\rangle_z$), and in some cases the axial direction as well (averaged quantity denoted by $\langle\cdot\rangle_{xz}$). Ensemble averaging was then performed over several realizations that were separated by a time greater than an estimated integral time scale of the flow (a spatial and ensemble-averaged quantity is denoted by $\langle\cdot\rangle_{xzt}$ or $\langle\cdot\rangle_{zt}$, where t denotes averaging over an ensemble of flow realizations, and the individual snapshots for ensemble averaging were separated by t_m as given in table 3). Statistics computed from averages in the azimuthal direction and not the axial direction (that is, $\langle\cdot\rangle_{zt}$), are referred to in this paper as having a two-dimensional

resolution, and statistics computed from averages in the azimuthal and axial directions are referred to as having a one-dimensional resolution (that is, $\langle\cdot\rangle_{xzt}$). The integral time scale was estimated using the inner cylinder velocity and circumference $2\pi R_1/W_1$. In this paper the notation $\langle\cdot\rangle$ is used interchangeably with $\langle\cdot\rangle_{xzt}$, and the notation $\langle\cdot\rangle_z$ is used interchangeably with $\langle\cdot\rangle_{zt}$ unless stated otherwise.

Velocity fluctuations at a point are defined according to the average in the azimuthal direction only ($u'' = u - \langle u\rangle_{zt}$, where u'' is the velocity fluctuation due to turbulence and u is the instantaneous velocity at a point) or the azimuthal and axial directions ($u' = u - \langle u\rangle_{xzt}$, where u' is the velocity fluctuation due to turbulence and the mean TV motion, referred to here as the velocity fluctuation, and u is the instantaneous velocity at a point). Special axial and radial coordinates are defined for reporting results. The axial coordinate x^* defines the axial location relative to the outflow of the first selected vortex pair from the inner cylinder ($x^* = 2x/\lambda(R_2 - R_1)$). The coordinate r^* defines a coordinate transform such that the wall-normal coordinate varies from zero to one ($r^* = (y - R_1)/(R_2 - R_1)$). Figure 1 illustrates these coordinate systems.

Wall shear stress is a vector quantity, but for the purposes of this paper only the shear stress in the azimuthal direction is considered. In terms of non-dimensional quantities the wall shear stress (normalized by ρW_1^2) is,

$$\tau_{yz_i} = \frac{1}{Re_1}\left(\frac{\partial w}{\partial y} - \frac{w}{y}\right)_i, \tag{4.1}$$

where the subscript i defines the inner or outer cylinder. Averaging in the axial and azimuthal direction and over the ensemble of samples was also applied to the wall shear stress. The same notation as that used for the velocity field averaging was applied, that is, $\langle\tau_{yz}\rangle_{xz}$ defines the instantaneous azimuthal component of shear stress averaged in the azimuthal and axial directions, and over an ensemble of samples.

Throughout this paper, units normalized by the friction velocity (referred to as wall units) are defined with a superscript $+$. A transform is performed such that $y_i^+ = 0$ corresponds to the wall. The subscript i refers to the cylinder that the coordinate is relative to and it also defines which wall (inner or outer cylinder) friction velocity is used to compute y_i^+. At the inner cylinder, the transform is (in terms of dimensionless quantities),

$$y_1^+ = r^* Re_{\tau_1}, \tag{4.2}$$

and at the outer cylinder, the transform is,

$$y_2^+ = (1 - r^*) Re_{\tau_2}, \tag{4.3}$$

where the friction-velocity-based Reynolds-number subscript designates the cylinder wall that the friction velocity is defined with respect to. That is, $Re_{\tau_i} = W_{\tau_i}(R_2 - R_1)/\nu$, where $W_{\tau_i}/W_1 = \sqrt{\tau_{yz_i}}$ (note that τ_{yz_i} is the dimensionless wall shear stress). The wall shear stress is defined according to (4.1) and in all instances in this paper averaging in the axial and azimuthal directions as well as over an ensemble of samples was applied for computation of the mean wall shear stress for defining wall units.

On some occasions when plotting results, the lower horizontal axis of a graph is used to define the coordinate r^*, whereas the upper horizontal axis is used for the wall-normal coordinate in wall units. The notation used for the wall units is relative to both the inner and outer cylinder in the format $y_1^+|y_2^+$ with the first listed coordinate being relative to the inner cylinder.

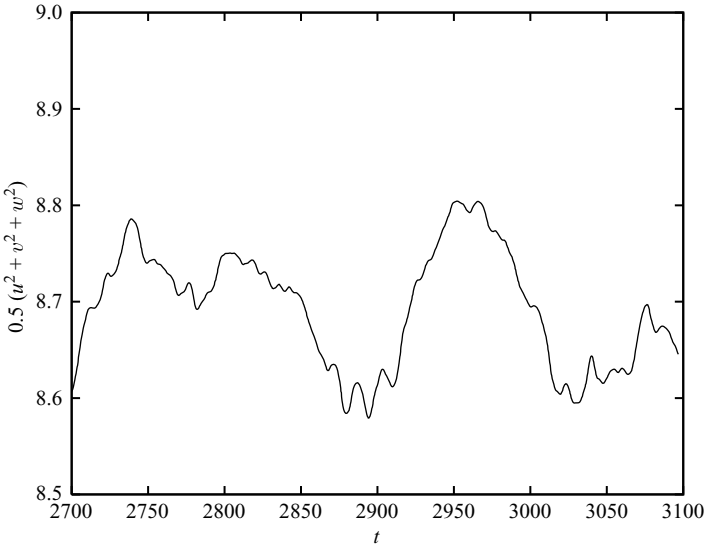

FIGURE 2. Total kinetic energy variation with time over the whole computational domain.

4.3. *Flow state confirmation*

Several tests were performed to confirm that a stationary flow state had been achieved. The first test identified a stationary state by the total (that is, the sum of the energy in each grid cell over the whole domain) kinetic energy remaining approximately constant. Figure 2 shows the kinetic energy variation with respect to time. There is a periodicity with a very long period of about 200 time units. Given that a cylinder rotation takes around 10 time units, and that the amplitude of the periodicity was small relative to the mean, this was not considered significant.

The next stationarity test looked at the variation of individual velocity components using a run test (Bendat & Piersol 1971). The run test was used because it does not require knowledge of the statistical distribution (e.g. Gaussian or otherwise) of the random variables in question. A time-based sequence of mean values is computed for different sample sizes and compared with the mean value of the entire data set. A run is counted as a sequence of successive mean values less than or greater than the mean of the entire data set. A confidence level of stationarity (that is, that the data does not exhibit any underlying trend) is then defined according to the number of runs r_s, and the number of samples N_s. A sample is then declared stationary at a given confidence level if the number of runs lies with a given range (Bendat & Piersol 1971). Table 4 summarizes the results for a run test of velocity components based on their mean square value with the fluctuation based on a purely time-averaged mean. That is, velocity components were monitored at selected points in the domain continuously in time and the signal was averaged over a continuous time sample. The results show that the velocity field is stationary for a 0.95 confidence interval for almost all of the trials based on the criteria for the number of runs given in notes b to d of table 4. The few cases that did not exhibit stationarity are not considered significant because the same velocity component was stationary for different sample sizes.

TC flow has been observed to be periodic and modulating in laminar flow states, particularly at higher laminar flow Reynolds numbers (Takeda 1999). Tests were undertaken to ensure that the flow state reached was showing features of

Velocity[a]	$N_s = 10$[b], $T_s = 42.71$	$N_s = 20$[c], $T_s = 21.25$	$N_s = 40$[d], $T_s = 10.68$
u_1[e]	$r_s = 8$	11	21
v_1	4	4	16
w_1	5	11	21
u_2[f]	5	13	21
v_2	3	11	19
w_2	7	13	17

[a] Total run time was 438.85 time units with 8.0×10^4 time steps.
[b] Requires $2 < r_s < 9$ for a 0.05 level of significance.
[c] Requires $6 < r_s < 15$ for a 0.05 level of significance.
[d] Requires $14 < r_s < 27$ for a 0.05 level of significance.
[e] Location 1 in y was midway between cylinders, x and z locations were arbitrary.
[f] Location 2 in y was close to the outer cylinder, x and z locations were arbitrary.

TABLE 4. Stationarity testing of velocity components. Number of runs r_s for a run test of velocity components based on the mean square of the velocity fluctuation over a number of samples N_s with sample period T_s.

Samples	Vortex	r_s, vortex size	r_s, vortex position
$N_s = 42$[a]	1	20	11
	2	16	15
	3	20	25
	4	20	21
$N_s = 72$[b]	1	35	15
	2	29	19
	3	31	16
	4	31	13

[a] 42 samples requires $14 < r_s < 27$ for a 0.05 level of significance.
[b] 72 samples requires $27 < r_s < 44$ for a 0.05 level of significance.

TABLE 5. Stationarity testing of the TV motion based on a run test for the TV size and location. Number of runs r_s based on number of samples N_s.

turbulent flow, without any periodic components due to modulation or TV axial movement.

The first test looked at the stationarity of the TV size and position. The mean vortex location was determined from the local maxima in $\langle v \rangle_z$ midway between the cylinders. The instantaneous vortex location was then found by averaging each flow realization in the azimuthal direction and determining the local maxima of $\langle v \rangle_z$. The spatial difference between local maxima indicated the vortex size for a velocity field at one instant in time. This was then compared with the mean vortex size and position for the entire set of data. Table 5 summarizes the results and notes a and b give the criteria for assessment of stationarity with a 0.95 confidence interval. It was found that the vortex size was stationary, but the vortex location was not stationary when a large sample size (72 as opposed to 42 samples) was used. That is, the vortices were found to have a statistical trend to suggest they were moving along the cylinder axis. The convection velocity of the vortices was calculated and found to be 1.19×10^{-4}. Over the duration of the simulation, this corresponds to the vortices moving 0.086 units in the axial direction, or about 4 grid nodes. The movement was considered sufficiently small to not have a major effect on statistics. When the vortex pair wavelength

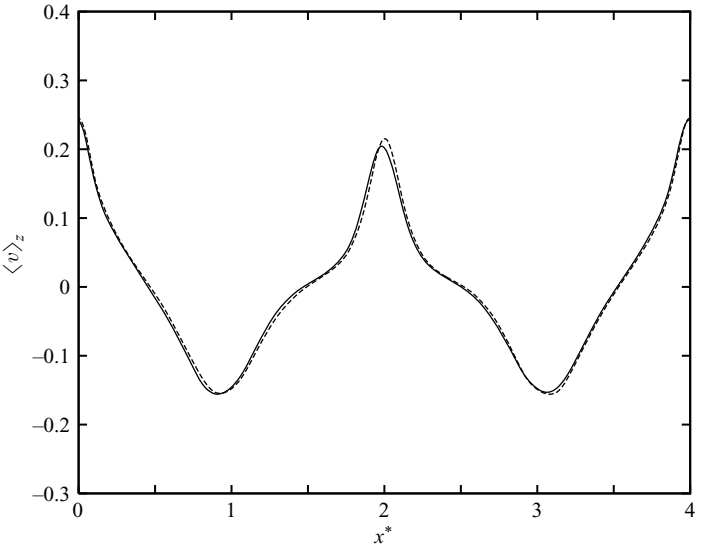

FIGURE 3. Movement of TV motion for a stationary case (- - -, 42 samples) and a non-stationary case (—, 72 samples). $r^* = 0.50$.

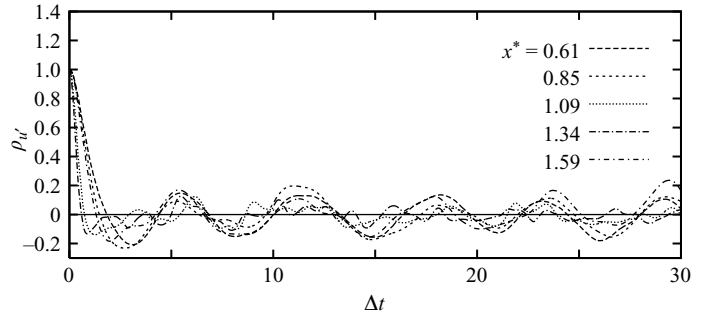

FIGURE 4. Autocorrelation of the velocity fluctuation, $u'' = u - \langle u \rangle_t$, at selected axial locations, mean velocity averaged in time only (that is, $\langle u \rangle_t$ is the velocity at a point averaged with respect to time). $r^* = 0.50$.

was calculated from the results, neglecting vortex movements, it was determined to be $\lambda = 2.2721$ and $\lambda = 2.3079$. This is a variation of only $\pm 0.78\,\%$ from the imposed wavelength of $\lambda = 2.29$. Finally, figure 3 shows the differences in $\langle v \rangle_z$ (midway between the cylinders) are minor for the stationary and non-stationary sample sizes.

The instantaneous data were also examined for periodic components. Figure 4 shows the autocorrelation for the axial velocity component (that is, u) with respect to time shift Δt at varying axial locations midway between the cylinders. There is a periodic component present at some axial locations with a period of approximately 5 time units. Visualization shows that the periodicity is probably due to pockets of positive and negative velocity fluctuations (figure 5). Local effects due to the periodicity can be neglected since the structure travels around the cylinder and for this work only the average effect around the cylinder circumference was of interest.

Gorman & Swinney (1982) observed modulation in laminar flow occurring as: a beating phenomenon, where the TV wavelength changes at every axial location

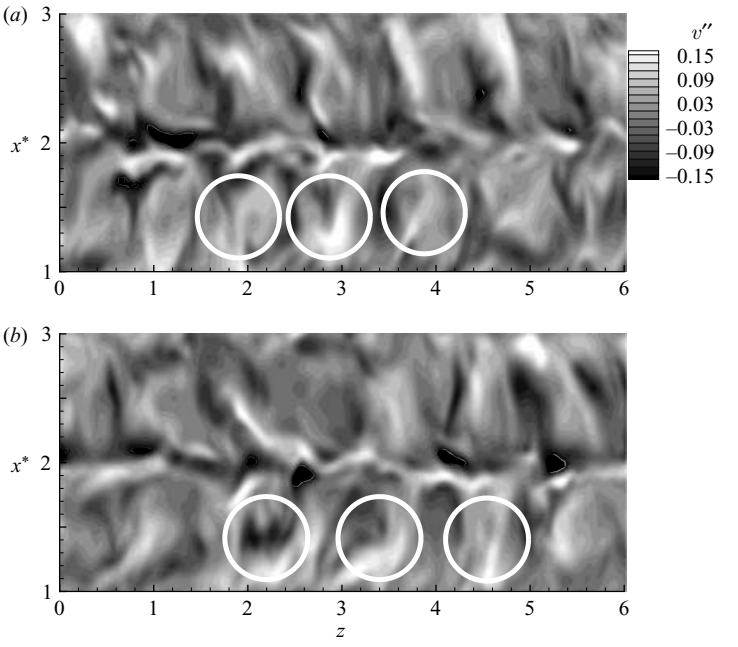

FIGURE 5. Visualization of the instantaneous velocity fluctuation v'' in the x^*–z plane with highlighting of an azimuthal structure. (*a*) $t = 0$, (*b*) 10.

simultaneously; a travelling phenomenon, where a wave in the form of local changes in the TV wavelength moves around the cylinder; and a combination of beating and travelling. For the present simulation, if modulation is of statistical significance it should be seen as a non-stationary trend in the velocity components. For each velocity field collected, a run test for stationarity was performed on the mean square velocity at axial locations corresponding to $x^* = 0.00, 0.25, 0.50, 0.75, 1.00, 1.25, 1.50, 1.75$ and 2.0, and eight equally spaced azimuthal locations were used (64 locations in total). The radial location was midway between the cylinders. All samples were found to be stationary according to run test criteria similar to those in tables 4 and 5, thus confirming that if modulation is present it is not of statistical significance for the present work.

Another important characteristic of the TV motion to consider was the symmetrical nature of the vortices within a vortex pair. Inspection of the mean velocity field (figure 6) shows that the vortices are approximately mirrored about the vortex outflow at $x^* = 2.0$ except for a minor shift.

There are several time scales for turbulent TC flow: the time for a revolution of the inner cylinder (10.1 time units); the time for a vortex to rotate about its axis; the time for an azimuthal structure to travel around the inner cylinder; the time for a vortex pair to travel a distance equal to its wavelength; and the time for the first zero crossing of the autocorrelation (an integral time scale of the flow, 2.5 time units, from figure 4). For sampling statistics a separation time of 10 time units was used. This time scale must be considered in relation to the flow time scales identified above.

The time between samples is much greater than the integral time scale and hence this is acceptable. A vortex revolution is dependent on the vortex radius (approximately 0.5 length units) and the radial velocity (approximately 0.225 units), and hence the time for a vortex revolution is 13.96 time units, assuming a circular vortex with

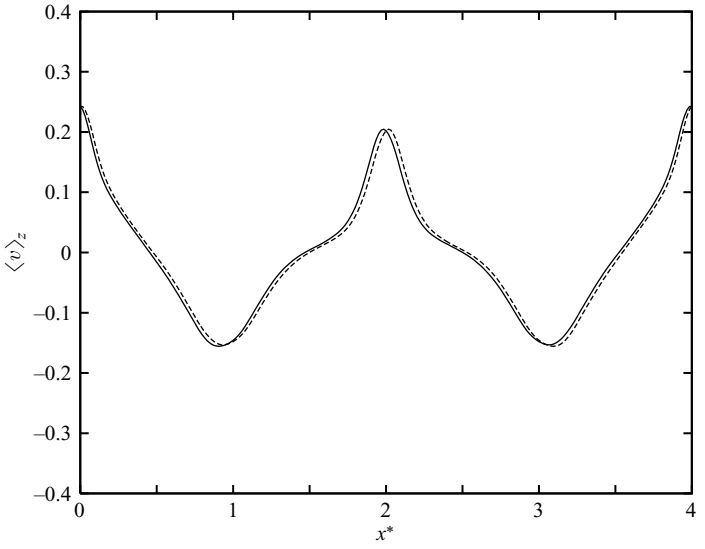

FIGURE 6. Comparison of – – –, mirrored profiles of $\langle v \rangle_z$ with —, non-mirrored profiles. $r^* = 0.50$.

constant angular velocity. The time between samples is less than this time scale. Since the statistics are processed in an Eulerian sense and averaged in the azimuthal direction, all possible points that a particle travelling around the vortex could occupy are considered. The azimuthal periodicity has a time scale of around 5.5 time units. If the data were sampled in phase with this, there is a potential problem as the data would be phase averaged. However, given that the data are also averaged in the azimuthal direction, and the periodicity is due to a structure travelling around the cylinder, the phase of the azimuthal wave is irrelevant with respect to the time between velocity samples.

The conclusion arising from this discussion is that the flow state is stationary and has the features of turbulent flow with a mean TV motion and there is an azimuthal periodicity present. Local effects due to the azimuthal periodicity can be neglected since the data are averaged in the azimuthal direction. The mean TV motion was found to be of a constant size, but moving slowly along the cylinder axis. However, the convection velocity of the mean TV motion was so small that it was assumed to have only a minimal effect on results. Further evidence of the existence of turbulence in addition to the TV motion is given in the next section by means of spectra.

4.4. *Grid resolution*

Grid resolution for the simulations was determined by matching the resolution in wall units to previous DNS studies of channel or pipe flow that used similar numerical methods at comparable Reynolds numbers (e.g. Kawamura *et al.* 1998). Table 6 summarizes the grid resolutions and domain sizes used by others.

One-dimensional energy spectra (based on azimuthal or axial separation) of velocity fluctuations (based on u'') were computed to verify adequate grid resolution. The spectrum was computed at radial locations $r^* = 0.039$ (near the inner cylinder), $r^* = 0.5$ (midway between the cylinders), and $r^* = 0.958$ (near the outer cylinder). Axial locations at $x^* = 0.00, 0.25, 0.50, 0.75, 1.00, 1.25, 1.50, 1.75$ and 2.00 were used for cases based on azimuthal separation.

Authors	Discretization, case	Streamwise	Wall-normal (min, max)	Spanwise
Present	Second order, TV flow	5.39, 8.74	0.35, 2.97	3.66
Loulou *et al.* (1997)	Spectral, pipe flow	9.9	0.39, 5.7	7.5
Eggels *et al.* (1994)	Second order, pipe flow	7.03	0.94, 1.88	0.05, 8.84
Moser & Moin (1987)	Spectral, curved channel flow	17.7	0.054, 4.4	5.9
Kawamura *et al.* (1998)	Second order, channel flow	9.0	0.4, 11.5	4.5

TABLE 6. Grid resolution (in wall units) used in previous DNS studies of channel and pipe flow.

Spectra based on azimuthal separation are shown in figure 7. At $r^* = 0.039$, the spectrum shows approximately seven orders of magnitude of decay, indicating that the grid resolution is sufficient to provide most of the energy dissipation. Some build-up of energy is observed for the higher wavenumbers, indicating that the grid could have been finer near the inner cylinder. Build-up of the spectrum is not always observed with DNS using second-order accurate discretization (Tafti 1996; Kravchenko & Moin 1997). In the present case, the grid is fine enough to minimize numerical error and allow some energy build-up to occur. In a DNS of turbulent pipe flow, Loulou *et al.* (1997) observed some energy build-up at high wavenumbers, but concluded that the overall consequence was not significant owing to the large overall decay of energy. Build-up of energy at high wavenumbers has been observed in other DNS studies (Moser & Moin 1987). All the statistics from these studies showed good agreement of first- and second-order statistics with experiment. As table 6 outlines, the current grid resolution is comparable to, or better than, previous second-order accurate DNS studies. The energy build-up is less noticeable at $r^* = 0.5$ and $r^* = 0.958$ as shown in figures 8 and 9, respectively. This is because the smallest length scales increase in size toward the outer cylinder. Evidence of this is seen in the lower value of friction-velocity-based Reynolds number toward the outer cylinder (table 7). The shape of the spectra in figures 7, 8 and 9 are generally similar to those found in turbulent shear flows, thus providing further evidence of turbulent velocity fluctuations in addition to the TV motion.

There is a small peak in the spectra at some axial locations. It occurs at a frequency of $k/2\pi r = 0.5$, which corresponds to a length of 1.05 radians in the azimuthal direction. This is comparable to the spacing of structures identified in figure 5.

The energy spectra for the axial separation are shown in figure 10. The behaviour of the spectra is similar to that observed for azimuthal separation, although much less pronounced in terms of the energy build-up at $r^* = 0.039$. There is a large decay of energy at all radial locations.

It was not possible to run a finer grid simulation (than the resolution given in table 3) because of computational limitations, and a coarse grid simulation was run instead. The coarse grid had 96 nodes in the axial direction, 48 nodes in the radial direction and 128 nodes in the azimuthal direction. In comparison, the grid for the present DNS had 256, 128 and 384 nodes in the axial, radial and azimuthal directions, respectively. Figure 11 shows spectra based on azimuthal separation for the two grids. Only a radial location midway between the cylinders was considered and only the axial velocity component was investigated. There is good agreement between the spectra for the large scales with the coarser grid giving slightly higher energy levels but a steeper rate of decay because of numerical dissipation. A comparison of velocity fluctuation levels at different grid resolutions is also made (figure 12).

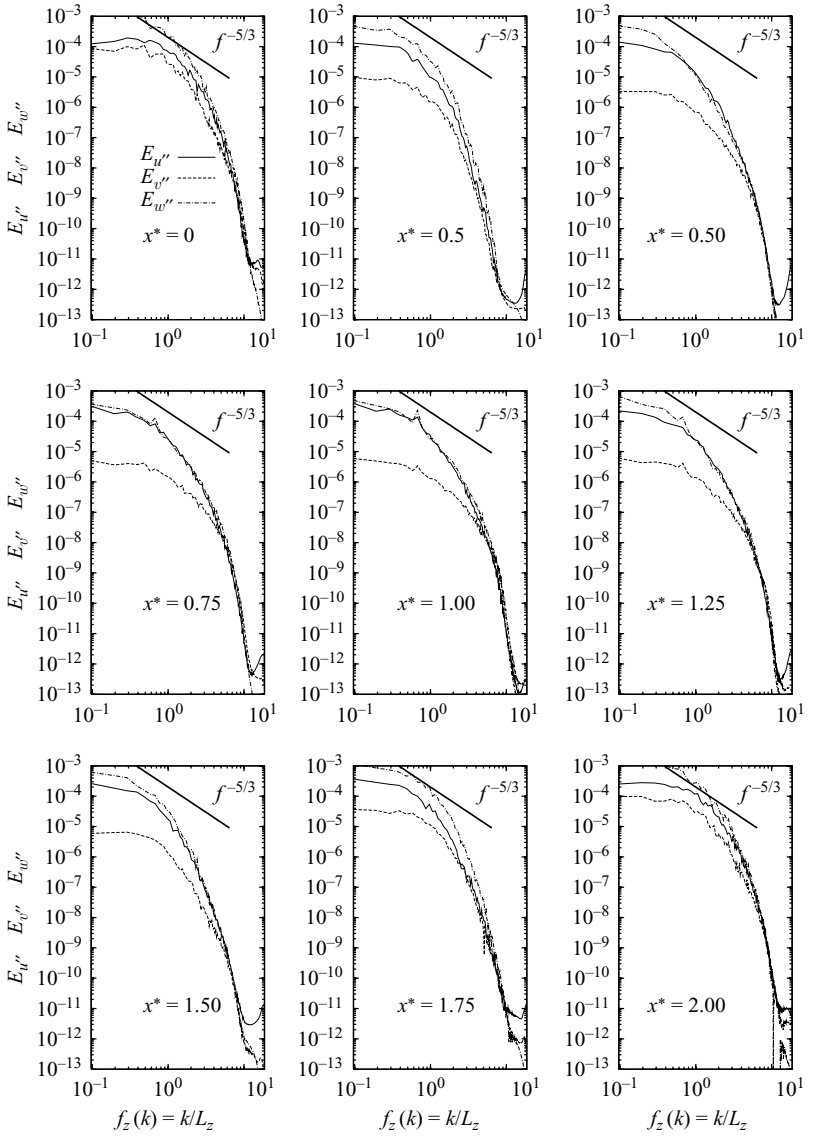

FIGURE 7. One-dimensional energy spectra of the velocity fluctuation based on azimuthal separation at $r^* = 0.039$. E is the energy, $f_z(k)$ is the frequency in direction z at wavenumber k, and L_z is the dimensionless domain length.

Generally, the agreement is poor near the inner cylinder where the length scales are smallest. The coarse grid tends to predict larger velocity fluctuation levels because of poor dissipation resolution. Toward the outer cylinder the agreement is improved.

4.5. *Comparison with experimental data*

The simulation was validated by comparison with available and applicable experimental results. Although there are many published experimental data related to turbulent TC flow, these data are spread over a range of Reynolds numbers and cylinder radius ratios that are impractical to reach using DNS. As a result, comparison

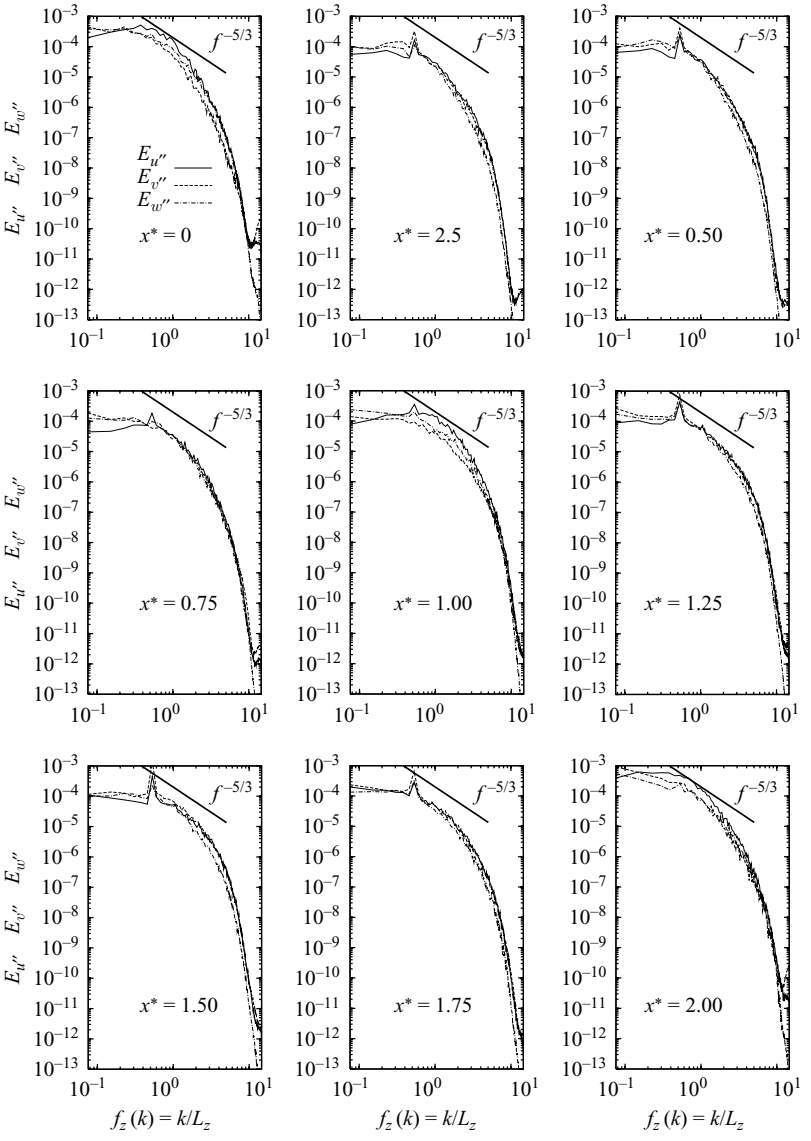

FIGURE 8. One-dimensional energy spectra of the velocity fluctuation based on azimuthal separation at $r^* = 0.5$. E is the energy, $f_z(k)$ is the frequency in direction z at wavenumber k, and L_z is the dimensionless domain length.

was made with available quantities that were based on experiments at similar, though not necessarily identical, Reynolds number and radius ratio.

Laminar flow simulations to predict the onset of laminar TV flow were undertaken as a validation test case. The theoretical critical Reynolds number (for the onset of laminar TV flow) at a radius ratio of $\eta = 0.617$ is $Re_1 = 72.7$ (DiPrima & Swinney 1981). In the simulations, a TV motion could be produced for a Reynolds number of 73.0, but it could not be produced at a Reynolds number of 72.8. This represents a variation from theory of 0.42%, and it was concluded that this verification was successful.

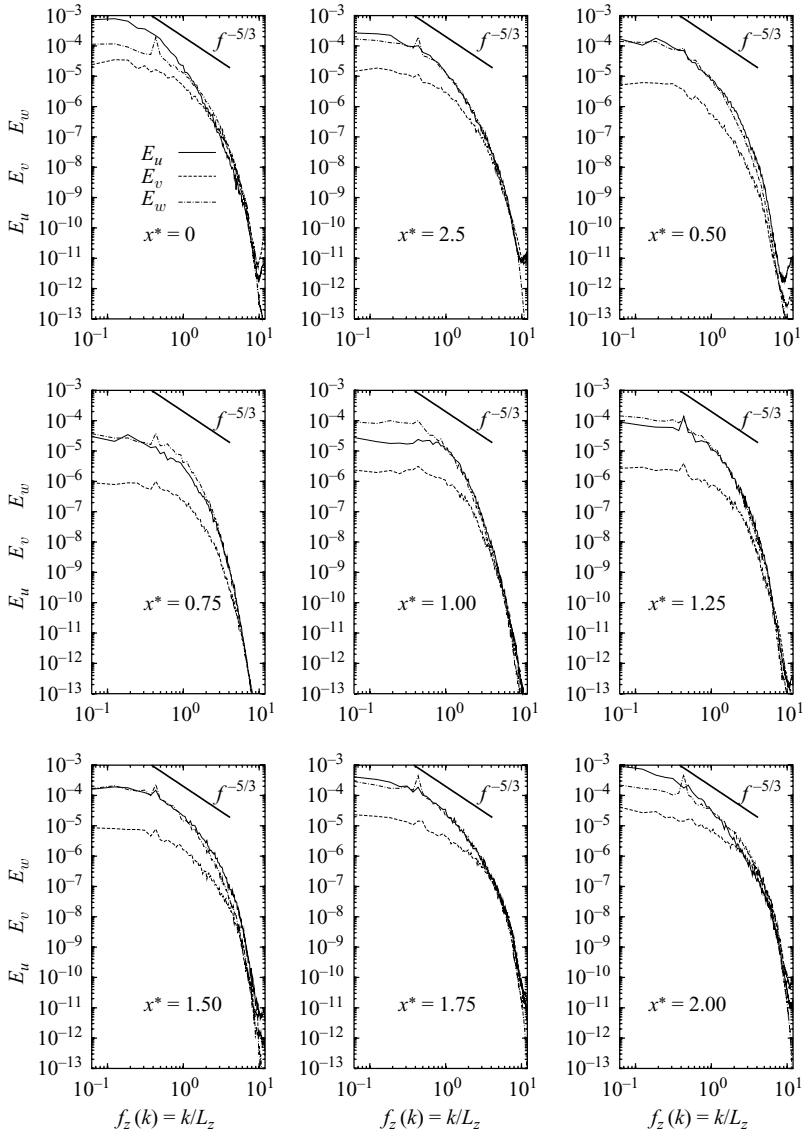

FIGURE 9. One-dimensional energy spectra of the velocity fluctuation based on azimuthal separation at $r^* = 0.958$. E is the energy, $f_z(k)$ is the frequency in direction z at wavenumber k, and L_z is the dimensionless domain length.

Integral flow parameters from the turbulent flow simulation are given in table 7. The total torque at the inner cylinder is also given, along with the torque based on an experimental correlation (Wendt 1933). The present work under-predicts the torque by around 8 %. This is probably because the extra torque due to the finite cylinder length (Wild *et al.* 1996) has not been accounted for in the DNS.

The mean velocity based on the one-dimensional resolution (as defined in § 4.2) is compared with experimental results (Smith & Townsend 1982) in figure 13. Despite the differences in the Reynolds number (for the experiment $Re_1 \approx 50\,000$) and the radius ratio (for the experiment $\eta = 0.66$), the results show similar behaviour. There

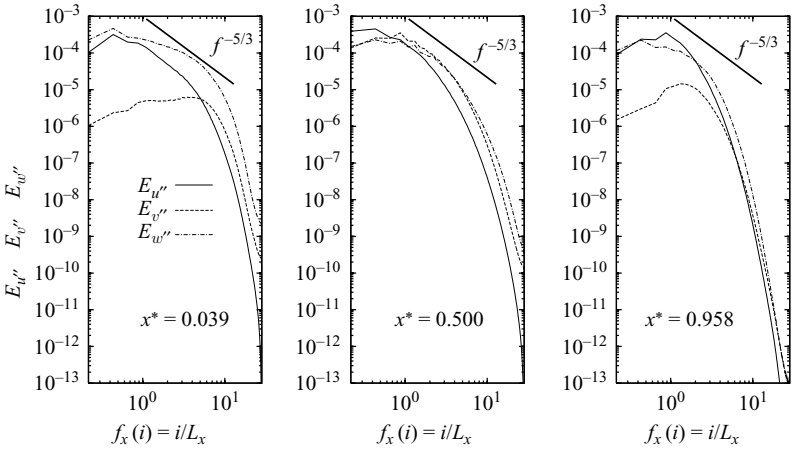

FIGURE 10. One-dimensional energy spectra of the velocity fluctuation based on axial separation. E is the energy, $f_x(i)$ is the frequency in direction x at wavenumber i, and L_x is the dimensionless domain length.

Re_1	$Re^a_{1_c}$	Re^*_1	Ta_1	Ta_2
3200	72.7	44	9.7×10^6	2521
$Re^{b,c,d}_{\tau_1}$	$Re^{b,c}_{\tau_2}$	G^{*d}_1	$G^{*d,e}_{1_{expt}}$	C^f_f
196.5	121.3	6.279×10^5	6.822×10^5	0.754×10^{-2}

[a] Critical Reynolds number for onset of laminar TV flow.
[b] $\langle \tau_{yz_i} \rangle = (1/Re_1)(\partial \langle w \rangle_i / \partial y - \langle w \rangle_i / y)|_{y=R_i}$.
[c] $W_{\tau_i}/W_i = \sqrt{\tau_{yz_i}}$.
[d] $G^*_1 = (Re_{\tau_1}(\eta/(1-\eta))^2)2\pi$, dimensionless torque at inner cylinder.
[e] Based on correlation from Wendt (1933).
[f] $C_f = 2(W^2_{\tau_1}/W^2_1)$.

TABLE 7. TC flow integral parameters.

are two distinct near-wall regions at each cylinder where there is a steep velocity gradient ($0 < r^* \lesssim 0.1$, $0.9 \lesssim r^* < 1$) due to the shear introduced at each cylinder wall. In the region midway between the cylinders ($0.1 \lesssim r^* \lesssim 0.9$), the magnitude of the velocity from DNS is less than in the experiment. The experiment also shows a slightly steeper near-wall velocity gradient due to the higher Reynolds number.

Mean velocity in a two-dimensional resolution is compared with experiment (Kobayashi *et al.* 1990) in figures 14, 15 and 16. The experiment was performed at a radius ratio of 0.92 and a Reynolds number of approximately 60 000. This is significantly different to the present DNS and it is a reasonable explanation for the differences observed. The trends are similar and the results show a weaker TV motion in the experiment owing to the higher Reynolds number. Unfortunately, there is no study as yet that provides the necessary information to perform scaling between different TC flow configurations in turbulent flow.

An additional component for validation, although not the topic of this paper, focused on passive scalar transport in turbulent TC flow. Scalar transport experiments (Kataoka *et al.* 1977) were used to guide the choice of radius ratio and Reynolds

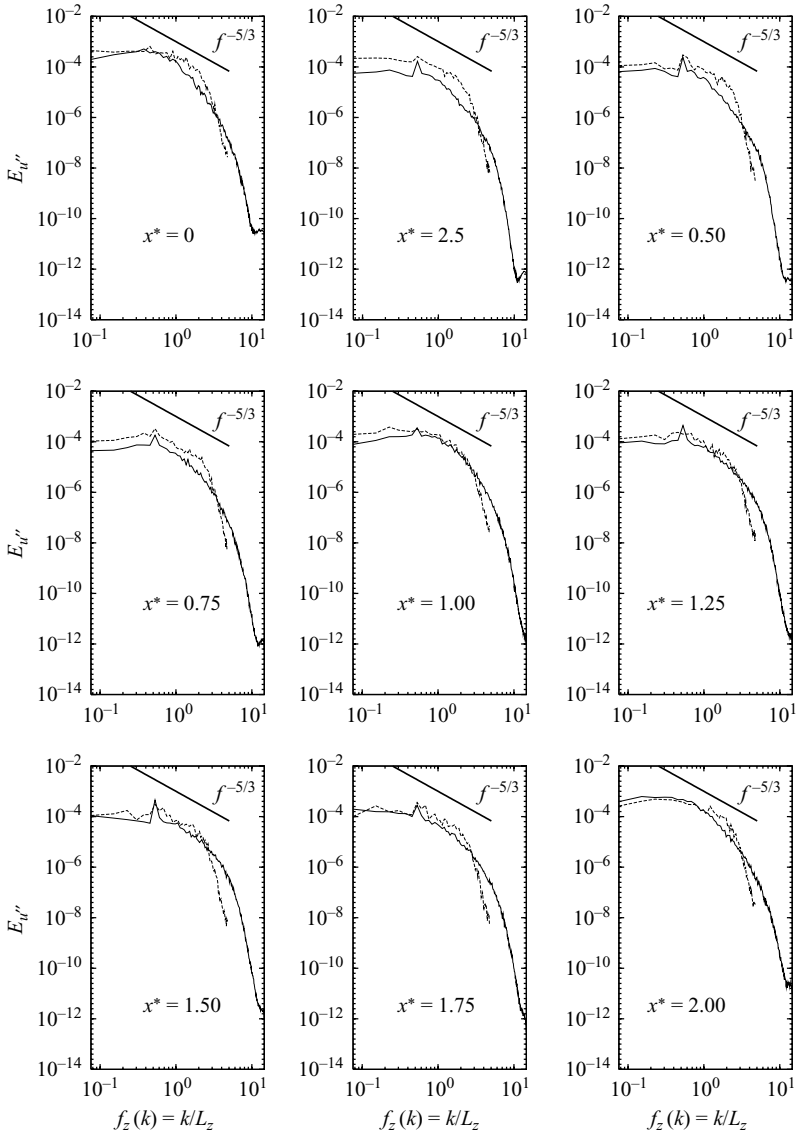

FIGURE 11. One-dimensional energy spectra of the velocity fluctuation based on azimuthal separation at $r^* = 0.5$ for comparison of —, the present DNS and - - -, coarse grid simulations. E is the energy, $f_z(k)$ is the frequency in direction z at wavenumbers k, and L_z is the dimensionless domain length.

number, and results from the experiment were used for validation of the present DNS. The governing equation for scalar transport is the conservation of species,

$$\frac{\partial c}{\partial t} + \nabla \cdot (\boldsymbol{u}c) = \frac{1}{ScRe_1} \nabla \cdot (\nabla c), \tag{4.4}$$

where c is the scalar concentration normalized by the difference between the inner and outer cylinder concentration, $Sc = \nu/\alpha$ is the Schmidt number, and α is the scalar diffusivity. The normalization and numerical method described in § 3 was used for the scalar equation. Boundary conditions were a fixed concentration of 1 at the inner

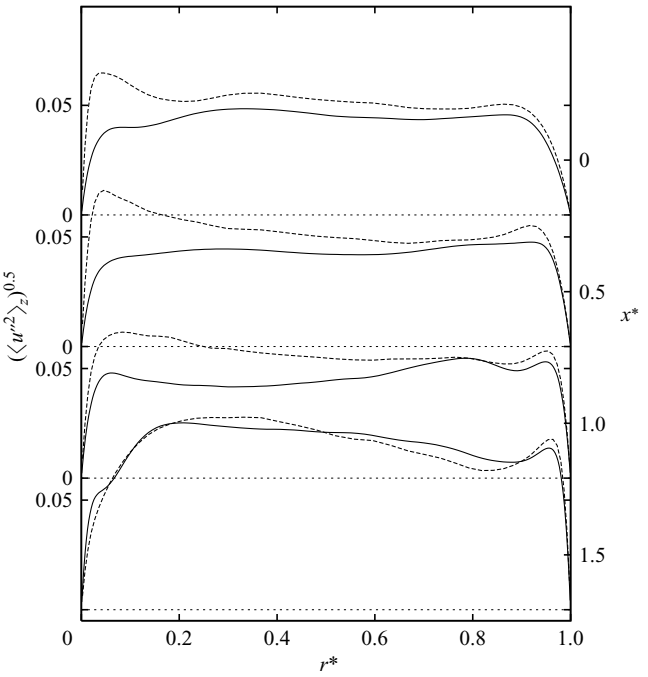

FIGURE 12. Fluctuating axial velocity, comparison of —, the present DNS and - - -, coarse grid simulations.

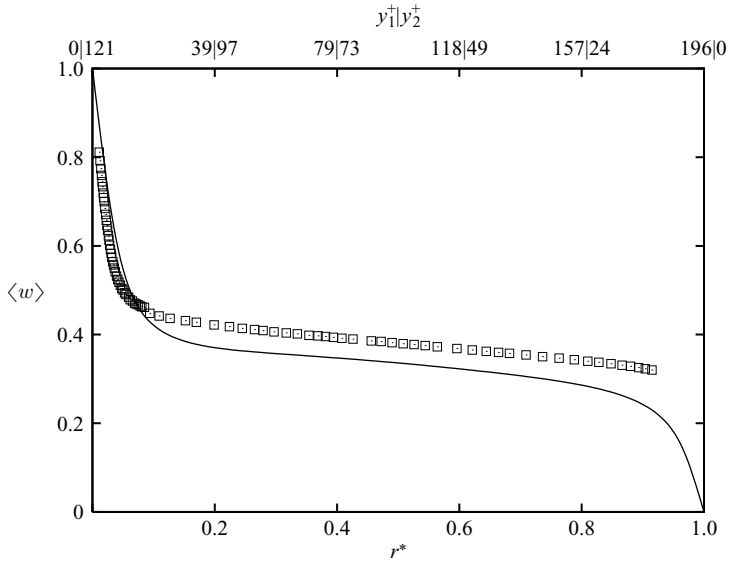

FIGURE 13. Mean velocity, one-dimensional resolution, comparison with experiment. —, DNS; ⊡, Smith & Townsend (1982).

cylinder and 0 at the outer cylinder. Schmidt numbers of 0.71 and 5.0 were considered. The quantity for comparison with experiment was the Sherwood number,

$$Sh = \frac{2k(R_2 - R_1)}{\alpha}, \tag{4.5}$$

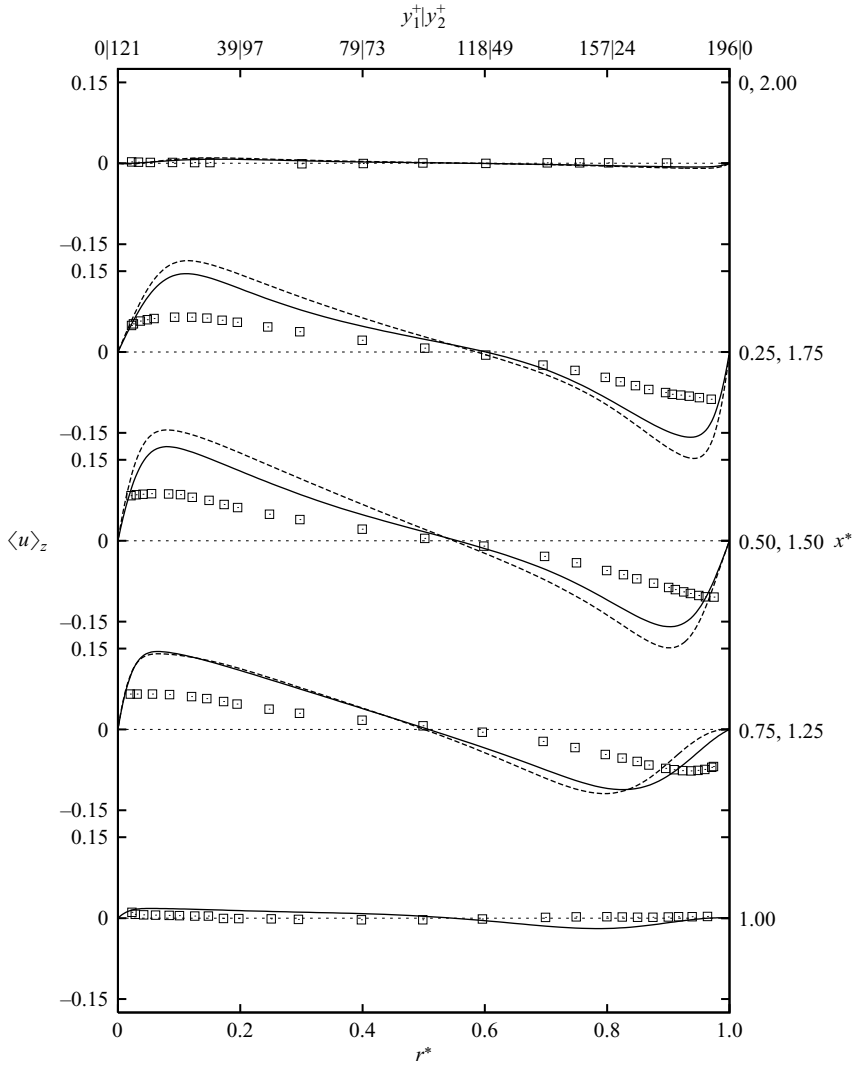

FIGURE 14. Mean velocity $\langle u \rangle_z$, two-dimensional resolution, comparison with experiment. —, present work ($x^* = 1.0$–2.0); - - -, present work ($x^* = 0$–0.75) ($-\langle u \rangle_z$); ⊡, Kobayashi *et al.* (1990).

where,

$$k = \frac{\alpha(\mathrm{d}c/\mathrm{d}y)_{wall}}{(c_1 - c_2)}. \tag{4.6}$$

Figure 17 shows the comparison with experiment (Sherwood number at the outer cylinder). Given that the experiment was done at a Schmidt number in the order of 3000 (too large to reach with DNS), the agreement between the experiment and DNS is very good. There is an improvement in the agreement for increasing Schmidt number. Additional results and discussion of the physical significance of results from the scalar transport studies are reported elsewhere (Bilson & Bremhorst 2003, 2004; Bilson 2004).

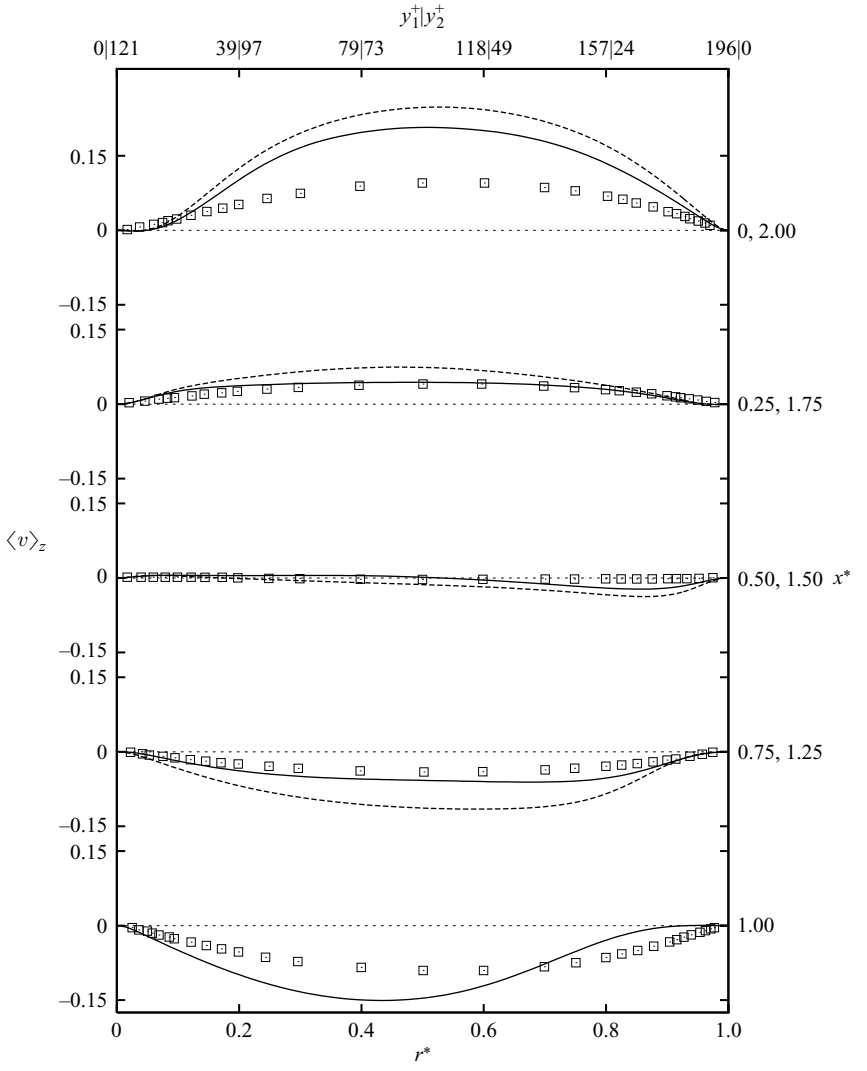

FIGURE 15. Mean velocity $\langle v \rangle_z$, two-dimensional resolution, comparison with experiment. —, present work ($x^* = 1.0$–2.0); - - -, present work ($x^* = 0$–0.75); ⊡, Kobayashi *et al.* (1990).

5. Results

5.1. *Mean velocity field*

Figures 14, 15 and 16 show the magnitudes of each mean velocity component in the radial and axial directions. Figure 18 shows stream traces based on the radial and axial velocity components representing the mean TV motion. The stream trace shows that two vortex pairs exist, with each pair having a wavelength of approximately $\lambda = 2$ when normalized by the vortex wavelength set at the start of the simulation. Additional, but smaller vortex pairs are present at the vortex inflow and outflow regions (inflows at $x^* = 1.0$ and $x^* = 3.0$ for the outer cylinder, and outflows at $x^* = 2.0$ and $x^* = 4.0$ for the inner cylinder, inflow and outflow refer to locations where the TV motion is toward or away from the inner cylinder). The primary vortex

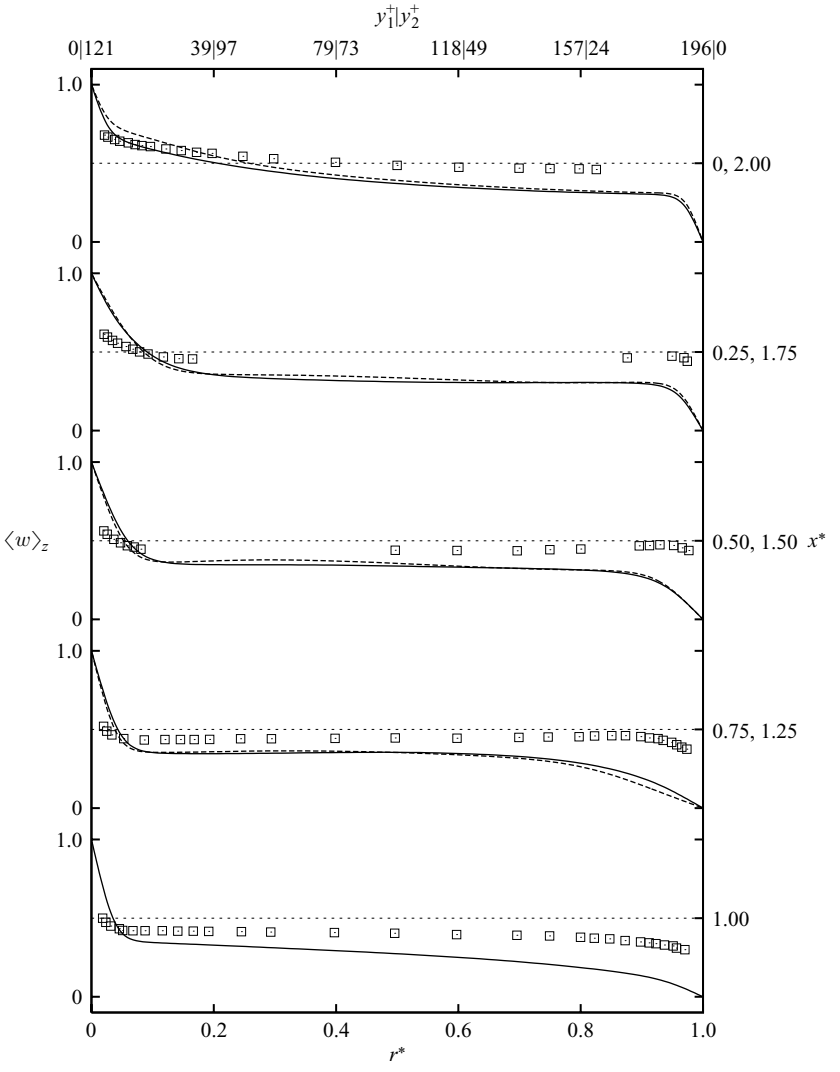

FIGURE 16. Mean velocity $\langle w \rangle_z$, two-dimensional resolution, comparison with experiment. Key as for figure 15.

pairs are expected as a result of the TV motion. The secondary vortex pairs have been previously identified based on Sherwood number (mass transfer rate) variations at the outer cylinder (Kataoka *et al.* 1977). They are formed as a result of shear between the two vortex pairs in the region where the primary vortex motion is away from either the inner cylinder or the outer cylinder. The secondary vortices appear to be similar to the GV motion identified experimentally in Barcilon & Brindley (1984). The primary and secondary vortex pairs give rise to variations of the mean shear stress along the axial direction of each cylinder surface, as shown in figure 19. This variation can also be linked to the mass transfer variation shown in figure 17 (Bilson & Bremhorst 2003).

A final mean velocity behaviour of interest is the near-wall velocity. Figure 20 shows the velocity near each cylinder wall in wall units. It is seen that the laminar sublayer region (that is, $\langle w \rangle^+ = y^+$) is maintained only very close to the wall ($y^+ \approx 2$).

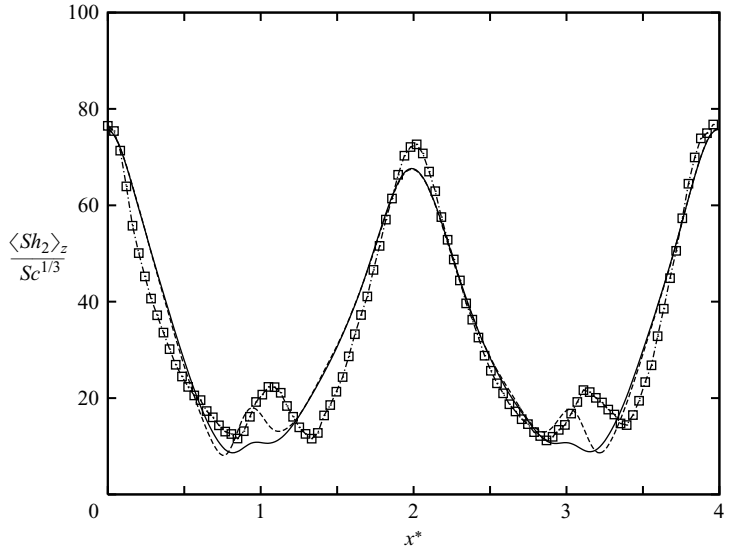

FIGURE 17. Sherwood number along axis of outer cylinder, comparison with experiment. —, $Sc = 0.71$; - - -, 5.00; ⊡ – · –, Katoaka *et al.* (1977).

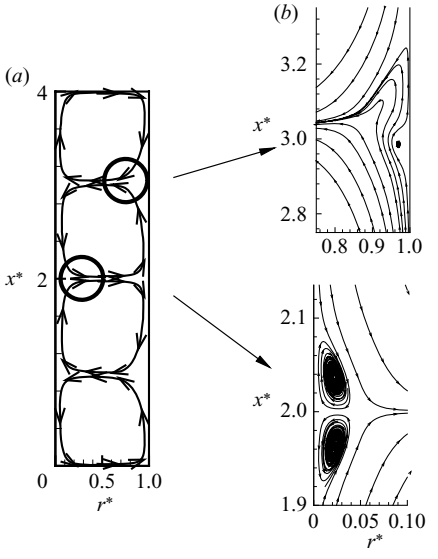

FIGURE 18. Stream traces from (*a*) the mean TV motion and (*b*) secondary vortex pairs.

5.2. *Fluctuating velocity statistics*

Fluctuating velocities, as defined in §4.2, are interpreted in terms of contributions from the mean TV motion and turbulence. Fluctuations due to turbulence and the mean motion are based on the u_i' velocity (that is, at a point $u_i' = u_i - \langle u\rangle$), whereas fluctuations due to turbulence alone are computed with the mean TV motion removed (that is, at a point $u_i'' = u_i - \langle u\rangle_{zt}$). This interpretation of velocity fluctuations consisting of turbulence and a mean TV motion is consistent with previous work

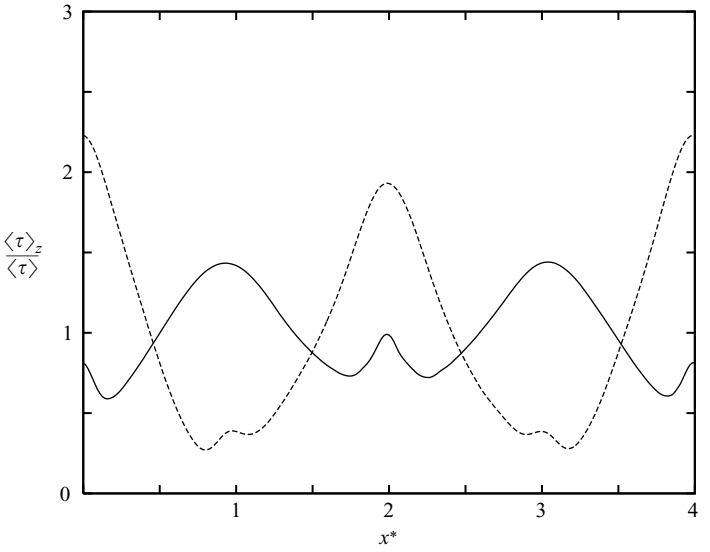

FIGURE 19. Wall shear stress at the inner and outer cylinders. —, τ_{yz_1}; - - -, τ_{yz_2}.

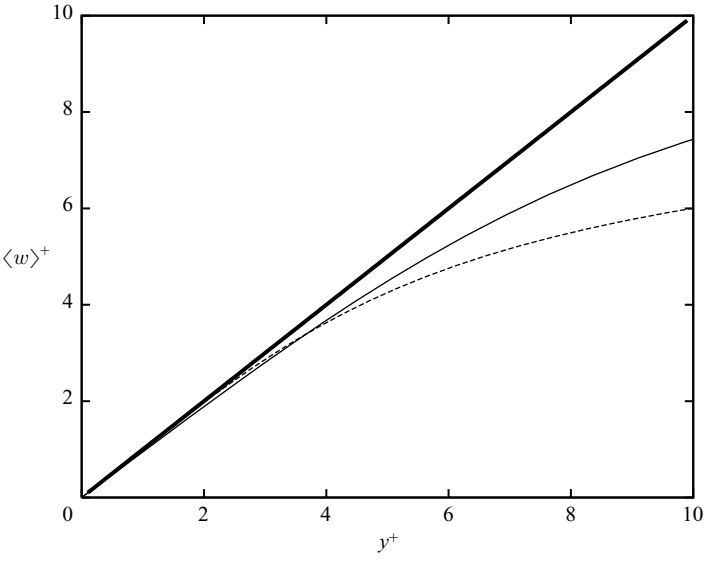

FIGURE 20. Mean velocity $\langle w\rangle^+$, wall units based on $\langle\tau_{yz_1}\rangle$ and $\langle\tau_{yz_2}\rangle$. —, inner; - - -, outer; —, $w^+ = y^+$.

(Smith & Townsend 1982). The two fluctuations are related according to,

$$\langle\langle u_i\rangle_z\langle u_j\rangle_z\rangle + \langle u_i'' u_j''\rangle = \langle u_i' u_j'\rangle + \langle u_i\rangle\langle u_j\rangle. \tag{5.1}$$

The fluctuations due to the mean TV motion and the turbulence are shown in figure 21. The total energy of the velocity fluctuations due to the mean TV motion and turbulence has two maxima (figure 21), one near the inner cylinder ($r^* \approx 0.1$) and one near the outer cylinder ($r^* \approx 0.9$). The magnitude of the fluctuation due to turbulence alone is lower than the fluctuation that includes turbulence and the mean TV motion, and there are no longer near-wall maxima in the profiles across the gap

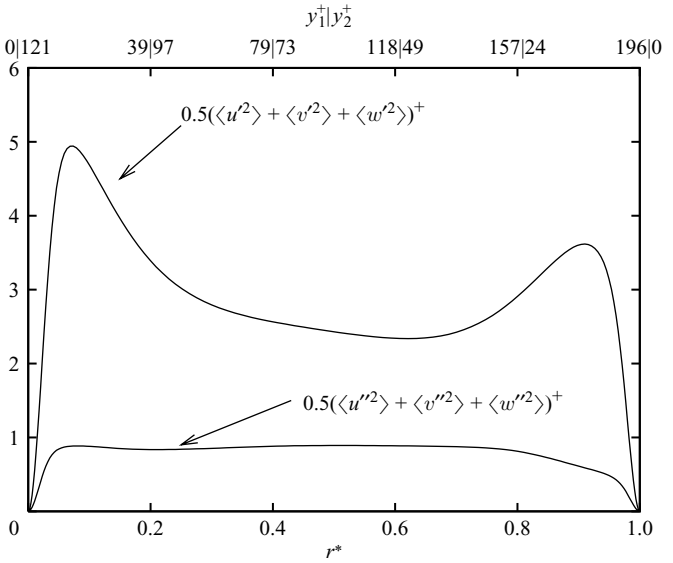

FIGURE 21. Kinetic energy of fluctuating velocity, including turbulence and mean TV motion, and turbulence alone, wall units based on $\langle \tau_{yz_1} \rangle$.

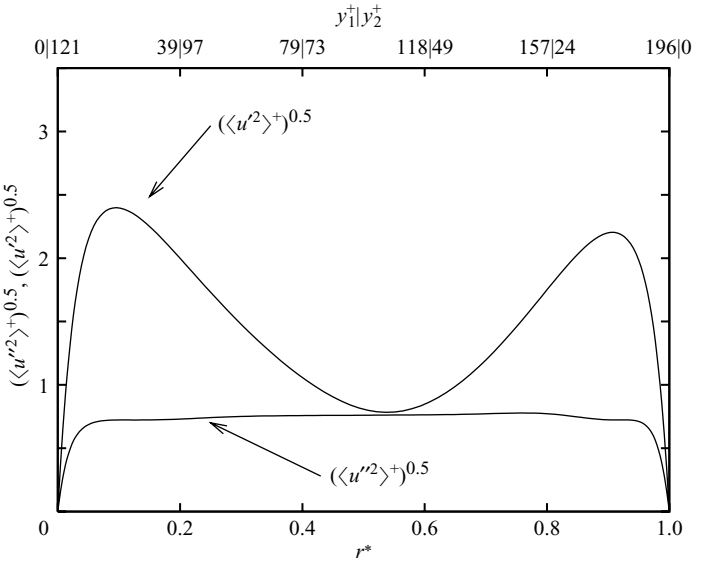

FIGURE 22. Fluctuating velocity for u' and u'', wall units based on $\langle \tau_{yz_1} \rangle$.

between the cylinders. It is clear that the TV motion makes a significant contribution to the velocity fluctuation.

A better understanding of the contribution of the TV motion can be achieved by considering the fluctuations for each individual velocity component. Axial velocity fluctuations due to turbulence (u'', figure 22) remain approximately constant for the cylinder gap width ($0.1 \lesssim r^* \lesssim 0.9$). The inclusion of the mean TV motion into the velocity fluctuation (u') shows a comparatively large contribution, especially near each wall where the axial velocity component is greatest as a result of the mean TV

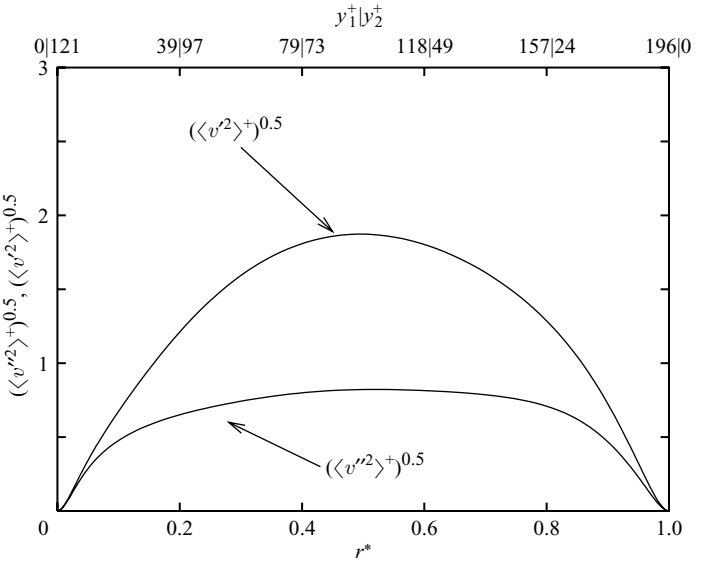

FIGURE 23. Fluctuating velocity for v' and v'', wall units based on $\langle\tau_{yz_1}\rangle$.

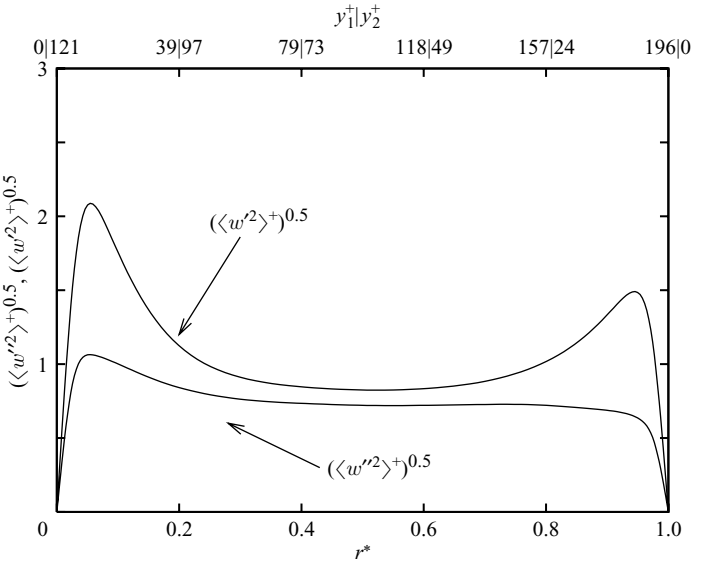

FIGURE 24. Fluctuating velocity for w' and w'', wall units based on $\langle\tau_{yz_1}\rangle$.

motion. The wall-normal fluctuations due to the turbulence and mean TV motion (v', figure 23) are greatest midway between the cylinders, with the TV motion contributing about two-thirds of the velocity fluctuation at $r^* \approx 0.5$. The turbulent component (v'') remains approximately constant across the cylinder gap width, with the exception of the near-wall regions. Streamwise velocity fluctuations, due to the turbulence and mean TV motion (w', figure 24), peak near the cylinder walls. Figures 21 to 24 also show that while the TV motion contribution is significant, it does not completely dominate the fluctuating velocity field.

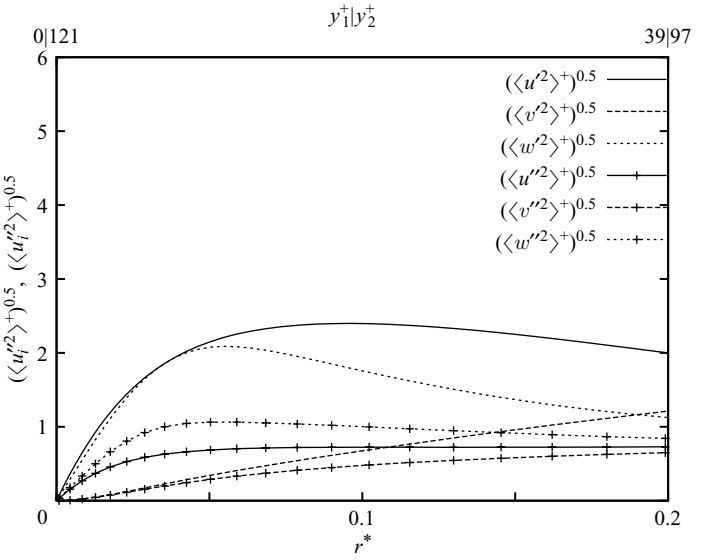

FIGURE 25. Fluctuating velocity near the inner cylinder, wall units based on $\langle \tau_{yz_1} \rangle$.

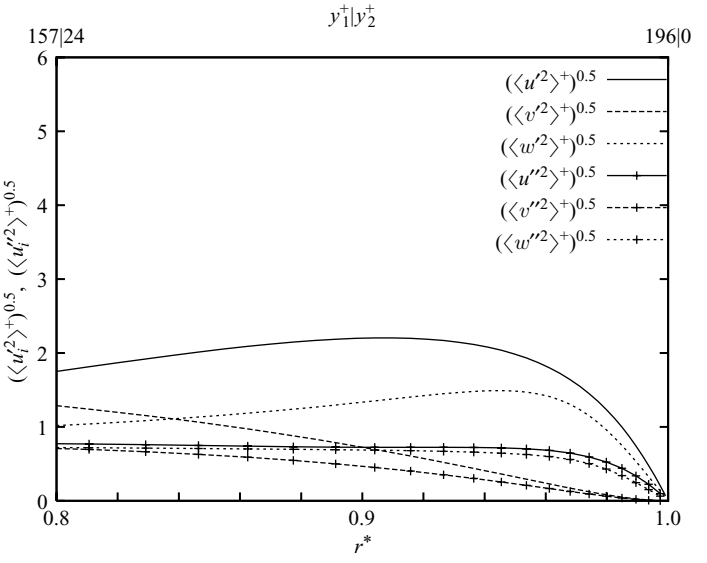

FIGURE 26. Fluctuating velocity near the outer cylinder, wall units based on $\langle \tau_{yz_1} \rangle$.

Near the walls, the contribution of the TV component to the fluctuations is greatest, whilst toward the centre of the gap width the TV component makes a relatively small contribution. The fluctuating velocity components all display similar behaviour and magnitudes away from the cylinder walls. The mean TV motion makes a large contribution to the velocity fluctuation and it is also observed near the inner and outer cylinders that $w' \approx u' \gg v'$, as observed in figures 25 and 26. This result is slightly different to plane boundary-layer flows such as pipe or channel flows

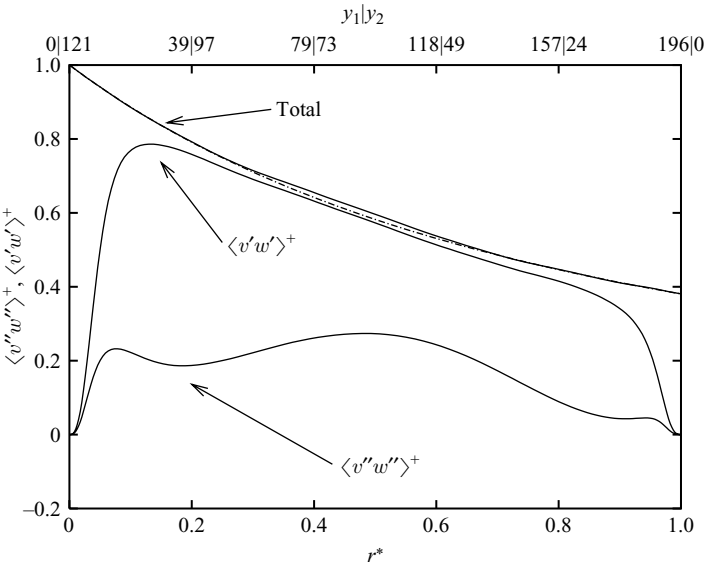

FIGURE 27. Fluctuating velocity for the Reynolds shear stress, wall units based on $\langle \tau_{yz_1} \rangle$. —, present work; – · –, R_1^2/y^2.

where typically $w' \gg u' \gg v'$. Similar behaviour is observed near each cylinder for the turbulent fluctuation where $u'' \approx w''$ and $u'' \approx w'' \gg v''$.

The maxima for the turbulent velocity fluctuations (in wall units) for streamwise, wall-normal and spanwise components are 1.0, 0.9 and 0.75, respectively, which is equivalent to a ratio of 1.33 : 1.2 : 1. In comparison with plane boundary layer flow, the ratio is 1.33 : 0.66 : 1 (Wilcox 1993). This indicates an enhanced wall-normal velocity fluctuation, which can be attributed to the mean TV motion increasing the production of these velocity fluctuations.

Figure 27 shows the shear stress variation between the cylinders. There is a theoretical balance between the shear stress due to velocity fluctuations (that is, Reynolds shear stress terms) and viscous effects,

$$\frac{y}{Re_{\tau_1}} \frac{\partial(\langle w \rangle^+/y)}{\partial y} - \langle v'w' \rangle^+ = \frac{R_1^2}{y^2}. \tag{5.2}$$

Figure 27 shows that the total shear stress variation across the cylinder gap width is in almost perfect agreement with the theoretical behaviour given in (5.2). There is a significant contribution to the shear stress by the mean TV motion and turbulent velocity fluctuations (that is, $\langle v'w' \rangle$) away from the cylinder walls. A large portion of this is due to the mean TV motion, as can be seen from the smaller magnitude of turbulent velocity fluctuations alone. This shows that the mean TV motion is responsible for much of the momentum transport from the inner to the outer cylinder.

The velocity fluctuations due to turbulence alone are shown in figures 28 to 30. In figure 28, there is clearly a non-uniform behaviour in u'' in the axial direction that is closely tied to the mean TV motion, as evidenced by the periodic nature of the fluctuations. At the vortex outflows (that is, TV motion is away from the inner cylinder) the fluctuation in u'' is greatest because of the higher shear and convection due to the mean TV motion in these regions. Similar trends are also observed for v'' (figure 29). At vortex inflows (that is, mean TV motion is toward the inner cylinder)

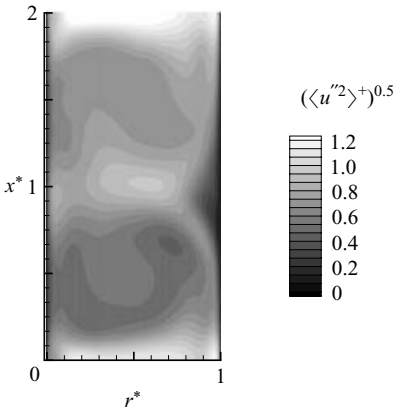

FIGURE 28. Fluctuating velocity u'', two-dimensional resolution, wall units based on $\langle\tau_{yz_1}\rangle$.

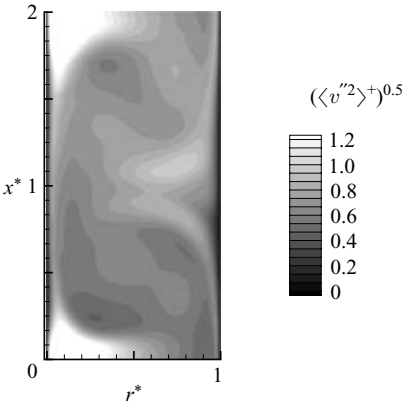

FIGURE 29. Fluctuating velocity v'', two-dimensional resolution, wall units based on $\langle\tau_{yz_1}\rangle$.

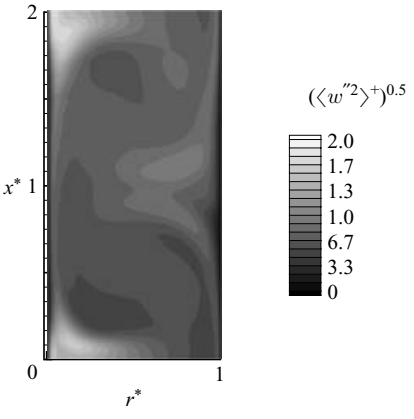

FIGURE 30. Fluctuating velocity w'', two-dimensional resolution, wall units based on $\langle\tau_{yz_1}\rangle$.

the fluctuation has a local minimum relative to other axial locations near the walls due to convection and turbulent transport of higher fluctuation fluid to regions away from the vortex outflows and inflows. Fluctuations of w'' show a region of large

w'' at the vortex outflows, however, this is not observed across the entire gap width (figure 30).

5.3. *Reynolds stress budgets*

Budgets of the Reynolds stress, due to the mean TV motion and turbulence (that is, the velocity fluctuation as defined by $u_i' = u_i - \langle u_i \rangle$) are reported in this section. The aim is to investigate how velocity fluctuations are produced, dissipated and transported across the gap between the cylinders. The equations describing the budgets include the budget for $\langle w'w' \rangle$,

$$
\begin{aligned}
0 = &-2\langle v'w' \rangle \frac{\partial \langle w \rangle}{\partial y} && (P_{ww}) \\
&-\frac{2}{y}\langle v'w' \rangle && (C_{ww}) \\
&-\left\{ \frac{1}{y}\frac{\partial (y\langle v'w'w' \rangle)}{\partial y} + \frac{2}{y}\langle v'w'w' \rangle \right\} && (T_{ww}) \\
&-\frac{2}{y}\langle v'p' \rangle && (PD_{ww}) \\
&+\frac{2}{y}\left\langle p'\left\{ \frac{\partial w'}{\partial z} + v' \right\} \right\rangle && (PS_{ww}) \\
&+\frac{1}{Re}\left\{ \frac{1}{y}\frac{\partial}{\partial y}\left(y\frac{\partial \langle w'w' \rangle}{\partial y} \right) - \frac{2}{y^2}(\langle w'w' \rangle - \langle v'v' \rangle) \right\} && (D_{ww}) \\
&-\frac{2}{Re}\left\{ \left\langle \frac{\partial w'}{\partial x}\frac{\partial w'}{\partial x} \right\rangle + \left\langle \frac{\partial w'}{\partial y}\frac{\partial w'}{\partial y} \right\rangle + \frac{1}{y^2}\left\langle \left(\frac{\partial w'}{\partial z} + v' \right)\left(\frac{\partial w'}{\partial z} + v' \right) \right\rangle \right\}, && (\epsilon_{ww})
\end{aligned}
\tag{5.3}
$$

the budget for $\langle v'v' \rangle$,

$$
\begin{aligned}
0 = &\frac{2}{y}\langle v'w' \rangle \langle w \rangle && (P_{vv}) \\
&+\frac{2}{y}\langle v'w' \rangle \langle w \rangle && (C_{vv}) \\
&-\frac{1}{y}\frac{\partial (y\langle v'v'v' \rangle)}{\partial y} + \frac{2}{y}\langle v'w'w' \rangle && (T_{vv}) \\
&-\left\{ 2\frac{\partial \langle v'p' \rangle}{\partial y} \right\} && (PD_{vv}) \\
&+2\left\langle p'\frac{\partial v'}{\partial y} \right\rangle && (PS_{vv}) \\
&+\frac{1}{Re}\left\{ \frac{1}{y}\frac{\partial}{\partial y}\left(y\frac{\partial \langle v'v' \rangle}{\partial y} \right) + \frac{2}{y^2}(\langle w'w' \rangle - \langle v'v' \rangle) \right\} && (D_{vv}) \\
&-\frac{2}{Re}\left\{ \left\langle \frac{\partial v'}{\partial x}\frac{\partial v'}{\partial x} \right\rangle + \left\langle \frac{\partial v'}{\partial y}\frac{\partial v'}{\partial y} \right\rangle + \frac{1}{y^2}\left\langle \left(\frac{\partial v'}{\partial z} - w' \right)\left(\frac{\partial v'}{\partial z} - w' \right) \right\rangle \right\}, && (\epsilon_{vv})
\end{aligned}
\tag{5.4}
$$

the budget for $\langle u'u' \rangle$,

$$
\begin{aligned}
0 = & -\frac{1}{y}\frac{\partial (y\langle u'u'v' \rangle)}{\partial y} && (T_{uu}) \\
& + 2\left\langle p'\frac{\partial u'}{\partial x} \right\rangle && (PS_{uu}) \\
& + \frac{1}{Re}\left\{ \frac{1}{y}\frac{\partial}{\partial y}\left(y\frac{\partial \langle u'u' \rangle}{\partial y} \right) \right\} && (D_{uu}) \\
& - \frac{2}{Re}\left\{ \left\langle \frac{\partial u'}{\partial x}\frac{\partial u'}{\partial x} \right\rangle + \left\langle \frac{\partial u'}{\partial y}\frac{\partial u'}{\partial y} \right\rangle + \frac{1}{y^2}\left\langle \frac{\partial u'}{\partial z}\frac{\partial u'}{\partial z} \right\rangle \right\}, && (\epsilon_{uu})
\end{aligned}
\tag{5.5}
$$

and the budget for $\langle v'w' \rangle$,

$$
\begin{aligned}
0 = & -\left\{ \langle v'v' \rangle \frac{\partial \langle w \rangle}{\partial y} - \frac{\langle w \rangle}{y}\langle w'w' \rangle \right\} && (P_{vw}) \\
& - \frac{\langle w \rangle}{y}\left\{ \langle v'v' - w'w' \rangle \right\} && (C_{vw}) \\
& - \frac{1}{y}\left\{ \frac{\partial (y\langle v'v'w' \rangle)}{\partial y} + (\langle v'v'w' \rangle - \langle w'w'w' \rangle) \right\} && (T_{vw}) \\
& - \left\{ \frac{1}{y}\frac{\partial (y\langle w'p' \rangle)}{\partial y} + \frac{2}{y}\langle w'p' \rangle \right\} && (PD_{vw}) \\
& + \left\langle p'\left\{ \frac{1}{y}\left(\frac{\partial v'}{\partial z} - w' \right) + \frac{\partial w'}{\partial y} \right\} \right\rangle && (PS_{vw}) \\
& + \frac{1}{Re}\left\{ \frac{1}{y}\frac{\partial}{\partial y}\left(y\frac{\partial \langle (v'w') \rangle}{\partial y} \right) - \frac{4}{y^2}\langle v'w' \rangle \right\} && (D_{vw}) \\
& - \frac{2}{Re}\left\{ \left\langle \frac{\partial v'}{\partial y}\frac{\partial w'}{\partial y} \right\rangle + \left\langle \frac{\partial v'}{\partial x}\frac{\partial w'}{\partial x} \right\rangle + \frac{1}{y^2}\left\langle \left(\frac{\partial v'}{\partial z} - w' \right)\left(\frac{\partial w'}{\partial z} + v' \right) \right\rangle \right\}, && (\epsilon_{vw})
\end{aligned}
\tag{5.6}
$$

where P_{ij} is the production term, C_{ij} the convection or bulk velocity gradient production term, T_{ij} the turbulence transport, PD_{ij} the pressure diffusion, PS_{ij} the pressure strain, D_{ij} the molecular diffusion, and ϵ_{ij} the dissipation. The subscript ij refers to the velocity components that the term represents. The budgets here are interpreted in the same manner as previously documented for turbulent shear flows.

Addition of the three velocity fluctuation component transport equations according to the definition of kinetic energy ($k = 0.5(\langle u'^2 \rangle + \langle v'^2 \rangle + \langle w'^2 \rangle)$) leads to the budget for the total fluctuation (figure 31). The peak of production (P_k) has a maximum near each wall and a small but constant value away from the walls. Near the inner cylinder, the peak is at $y_1^+ \approx 8$, which is comparable to a boundary-layer flow where the peak is at $y^+ \approx 10$. However, at the outer cylinder, the peak is at $y_2^+ \approx 5$. Production in turbulent TC flow is due to interaction of the mean streamwise velocity gradient and Reynolds shear stress (see (5.3)). The velocity gradient is responsible for the peak in production near the inner cylinder. Across the cylinder gap width, the production approaches a small but constant value because a velocity gradient remains. There are bulk velocity gradient effects (that is, production due to terms of the form $\langle u_i'u_j' \rangle \langle u_i \rangle / y$) that are included in the interpretation of the production term and hence make a positive contribution (see, for example, P_{vv} in (5.4)). Local equilibrium (production equal to

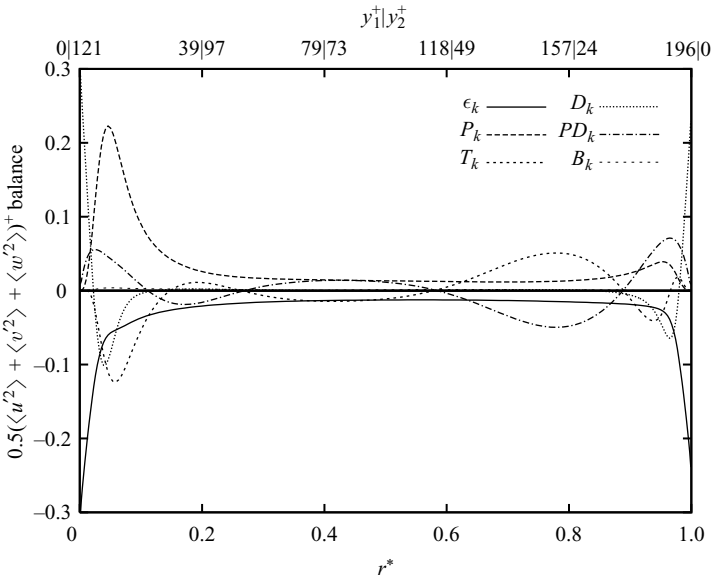

FIGURE 31. Total velocity fluctuation budget, wall units based on $\langle \tau_{yz_1} \rangle$.

dissipation) is achieved in the regions away from the cylinder walls ($0.2 \lesssim r^* \lesssim 0.9$). Equations (5.3) and (5.4) have a number of terms which are equal and opposite, namely $C_{ww} = -C_{vv}$ and the second terms of T_{ww} and D_{ww} have equal and opposite counterparts in T_{vv} and D_{vv}. These terms are indicative of direct energy interchange, or redistribution, by turbulent and molecular diffusion between the w' and v' velocity fluctuations.

For near-wall regions ($0 < r^* \lesssim 0.2$ and $0.9 \lesssim r^* < 1$), dissipation (ϵ_k) approaches its maximum value (acting as a loss) as the wall is approached. Very close to the wall, dissipation is balanced by viscous diffusion (D_k). The viscous diffusion transport mechanism brings high-velocity fluctuation fluid close to the walls (that is, in the region $r^* \lesssim 0.05$ and $r^* \gtrsim 0.95$). In regions slightly further away from the walls ($0.05 \lesssim r^* \lesssim 0.1$ and $0.9 \lesssim r^* \lesssim 0.95$), the viscous diffusion acts to move high-velocity fluctuations away from the region owing to the high rate of change of gradients associated with production, and hence it represents a loss.

Turbulent transport (T_k) terms also play a role in the budget. Near the inner cylinder ($0 < r^* \lesssim 0.15$), the turbulent transport acts as a loss to move velocity fluctuations away. This is due to the high gradients associated with production of velocity fluctuations in this region coupled with the TV motion away from the inner cylinder. Near the outer cylinder, turbulent transport also acts as a loss, moving fluctuations away from the region $0.85 \lesssim r^* \lesssim 0.95$. Closer to the wall, turbulent transport then acts to deliver a gain in fluctuations to the outer cylinder.

Since products of pressure and strain rate represent redistribution of energy amongst components of velocity fluctuations, only PD_{vv} represents a loss or gain of energy from the flow. Consequently, the pressure (PD_k) terms in turbulent TC flow act as a gain near the inner cylinder (the PS_k terms are zero as a result of continuity). This is due to the high-pressure region pushing higher velocity fluctuation fluid closer to the wall. For $0.15 \lesssim r^* \lesssim 0.9$, the pressure terms and turbulent transport approximately mirror each other, alternatively acting as gains and losses. This can be interpreted as turbulence causing a local acceleration and deceleration of the fluid, leading to local changes in the pressure field, which subsequently resists changes in the velocity

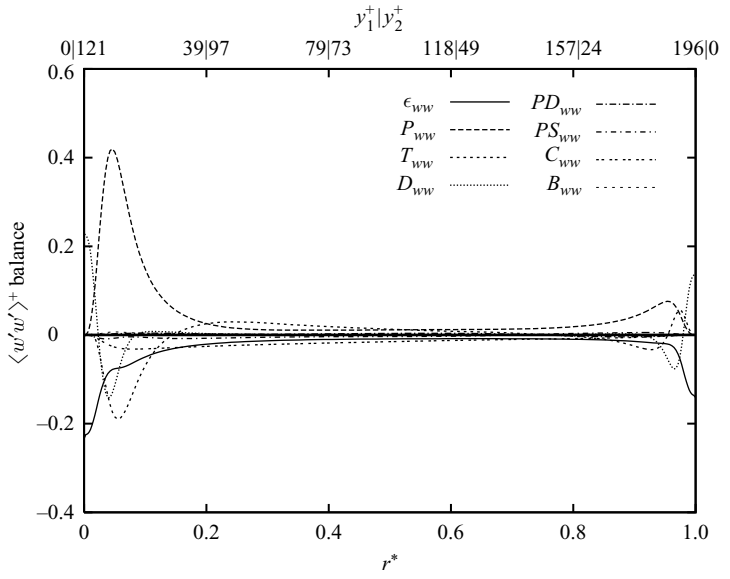

FIGURE 32. Reynolds stress budget, $\langle w'w' \rangle^+$ wall units based on $\langle \tau_{yz_1} \rangle$.

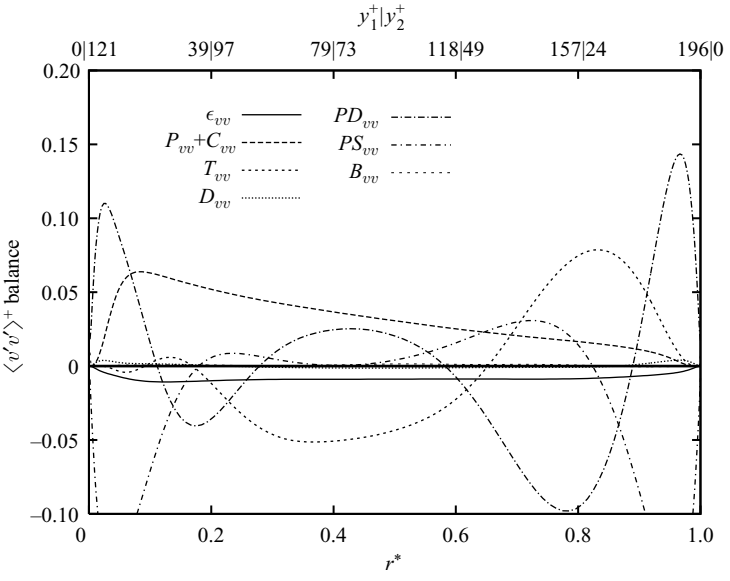

FIGURE 33. Reynolds stress budget, $\langle v'v' \rangle^+$ wall units based on $\langle \tau_{yz_1} \rangle$.

(Bradshaw 1971, Chapter 2 and Appendix 1). The balance term B_k reflects any imbalance due to numerical effects and it is noted that it is negligibly small.

Production of the velocity fluctuation is seen to be dominated by the production of $\langle w'w' \rangle$, which is due to the interaction of the Reynolds shear stress with the mean velocity gradient (figure 32). There is also a loss in the $\langle w'w' \rangle$ budget due to the bulk velocity gradient (C_{ww}), however, this term re-appears as a gain in the $\langle v'v' \rangle$ budget, equation (5.4) and figure 33 (C_{vv}), thus representing an interchange of energy between v' and w'. Other terms in the budget show similar behaviour to their analogous terms in the total fluctuation budget (refer to figure 31), with the exception of pressure and

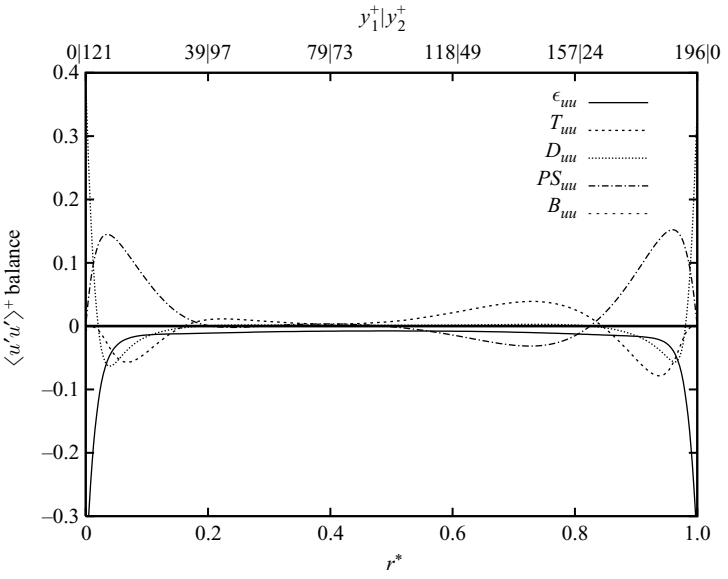

FIGURE 34. Reynolds stress budget, $\langle u'u'\rangle^+$ wall units based on $\langle \tau_{yz_1} \rangle$.

dissipation. Dissipation has a slight change in the slope of the profile at $r^* \approx 0.05$. Pressure terms are negative but small, indicating that pressure is still responsible for the volume deformation mechanism of transferring velocity fluctuations to other components, as it is in plane channel or pipe flow (Bradshaw 1971), but to a lesser extent. Most of the production of velocity fluctuations in the streamwise direction is balanced by dissipation; however, some additional transport mechanisms act to produce velocity fluctuations in the other two velocity components.

Velocity fluctuation gain terms for the wall-normal velocity fluctuation are due to interaction of the bulk velocity gradient ($\langle w \rangle / y$) and Reynolds stress (represented by P_{vv} and C_{vv} in (5.4) and in figure 33). Additional gains and losses are due to the pressure terms (PD_{vv}, PS_{vv}). The pressure terms are a significant component of this budget. The pressure terms tend to act as losses near each cylinder ($0 < r^* \lesssim 0.3$ and $0.6 \lesssim r^* < 1$). Near the outer cylinder, pressure terms are approximately balanced by turbulent transport (T_{vv}), indicating a situation where the turbulent transport causes volume deformation and generates an associated pressure field to oppose velocity fluctuations. The dissipation (ϵ_{vv}) is generally small for $\langle v'v' \rangle$, and it becomes negligibly small near the walls thus indicating that the effect of v' is to redistribute fluctuating velocity components. Viscous diffusion (D_{vv}) is also relatively small in this region. This is due to the physical influence of the cylinder wall. The combination of the no-slip condition and continuity results in a zero gradient of wall normal velocity at the wall ($\partial v'/\partial y = 0$) and also a small value of v'.

The u velocity is in a coordinate direction for TC flow that is analogous to the spanwise direction in a plane boundary layer flow (that is, plane channel, pipe or boundary layer). As in plane boundary-layer flows, there are no net production terms for the $\langle u'u' \rangle$ budget (5.5). However, this is not necessarily the case for TC flow as the vortices do create shear and hence turbulence, but the axial average which includes the effect of turbulence as well as the mean TV motion removes the evidence of this effect in the results. The major source of $\langle u'u' \rangle$ is from the pressure term (PS_{uu}) through the u' fluctuation (figure 34). The pressure term PD_{vv} peaks near the inner cylinder at $y_1^+ \approx 5$ and near the outer cylinder at $y_2^+ \approx 5$. These locations are

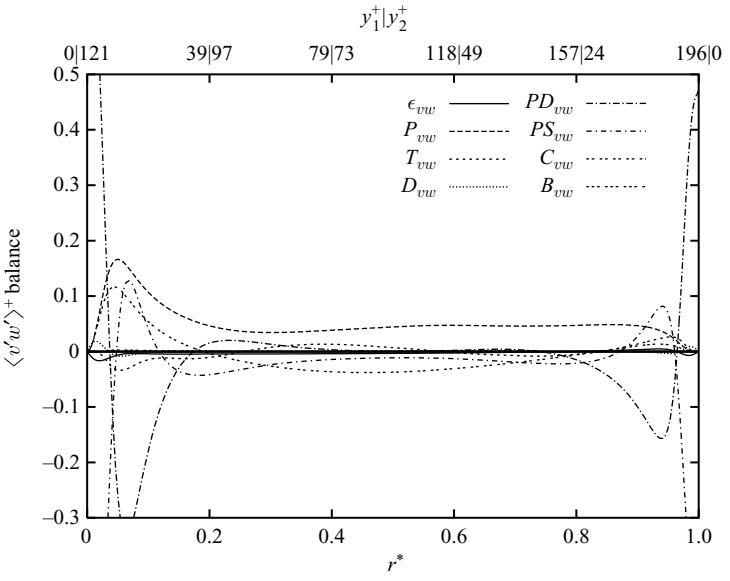

FIGURE 35. Reynolds stress budget, $\langle v'w' \rangle^+$ wall units based on $\langle \tau_{yz_1} \rangle$.

slightly nearer to the wall compared to those locations observed for the total velocity fluctuation in figure 31. Pressure gain terms occur because of elongation in the axial direction (that is, a shear effect of the TV motion) of the fluid element by local changes in pressure that occur owing to streamwise velocity fluctuations. For the $\langle v'v' \rangle$ budget, the pressure terms had an approximately equal value to those of the $\langle u'u' \rangle$ budget (that is, the PS_{vv} term in (5.4)), although in areas where PS_{uu} was positive, PS_{vv} tended to be negative owing to continuity, and vice versa when PS_{uu} was negative. The consideration of continuity leads to the conclusion that azimuthal and wall normal velocity fluctuations are largely responsible for generation of axial velocity fluctuations. It is likely that this mechanism would be dominated by the TV motion. Diffusion and dissipation balance at the walls. The diffusion is positive at the walls owing to the large near-wall value of $\langle u'u' \rangle$. Turbulent transport acts to redistribute fluctuations away from either wall, an indication that wall normal fluctuations move axial velocity fluctuations away from regions of large axial velocity fluctuation.

The budget of the Reynolds stress $\langle v'w' \rangle$ is dominated by production (P_{vw}), bulk gradient production (C_{vw}), and pressure terms (PS_{vw}, PD_{vw}) (figure 35). Other terms due to dissipation, viscous diffusion and turbulent transport are non-zero, but substantially smaller in magnitude. Production is due to the local mean velocity gradient as well as the bulk gradient, represented by $\langle w \rangle / y$, and its interaction with $\langle w'w' \rangle$ resulting from cylinder rotation. Bulk velocity gradient terms actually have a loss effect midway between the cylinders ($0.2 \lesssim r^* \lesssim 0.8$) and this is attributable to the TV motion (that is, large values of $\langle v \rangle_z$ in this region). Pressure terms act as losses in this budget, resisting the production mechanisms discussed above.

The Reynolds stress budgets for the turbulent TC flow have shown that pressure plays a more complex and different role in the budget compared with its role for plane boundary layer type flows (that is, boundary layer, channel or pipe flow). There is still pressure transfer from the streamwise velocity fluctuation, but it is small compared with other terms. In the wall normal velocity fluctuation budget, dissipation is minimal and pressure terms act to transfer some of the velocity fluctuations. Production of velocity fluctuations occurs through a mean field interaction effect (identified as C_{vv})

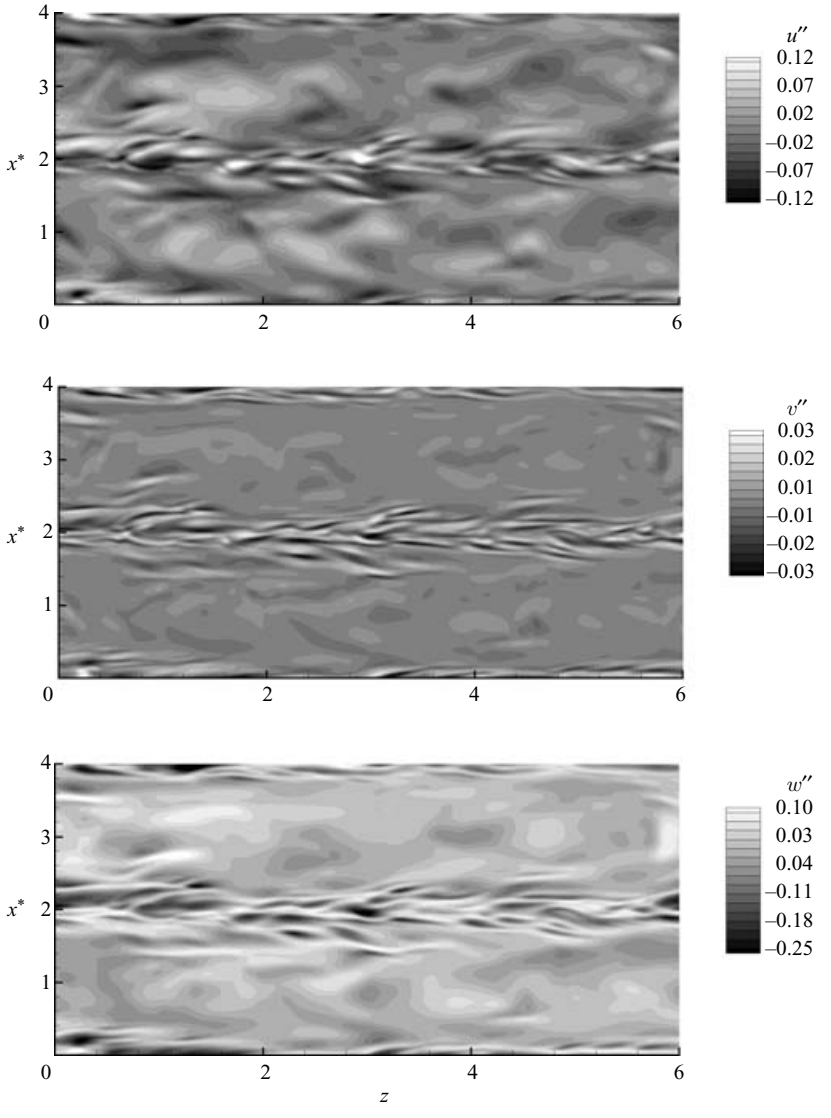

FIGURE 36. Visualization of velocity fluctuations in the x^*–z^* plane at $y_1^+ = 3.46$.

as well as a result of the local gradient of mean velocity. Pressure terms are seen to be the main source of spanwise velocity fluctuations.

5.4. *Visualization of the instantaneous velocity field*

Instantaneous velocity fields are examined in this section using flow visualization. A wide variety of visual work exists for TC flow; however, much of this work focuses on the TV flow state and it is generally restricted to the surface of the outer cylinder or a single azimuthal plane. With DNS, several different viewing angles and viewing planes can be applied simultaneously, thus making it a very powerful visualization tool.

Figure 36 shows velocity fluctuations in u'', v'' and w'' at $y_1^+ = 3.46$ (that is, close to the inner cylinder). Streaks of positive and negative velocity fluctuations are observed, but unlike plane boundary layer flow (that is, flat plate, pipe or channel flows), the

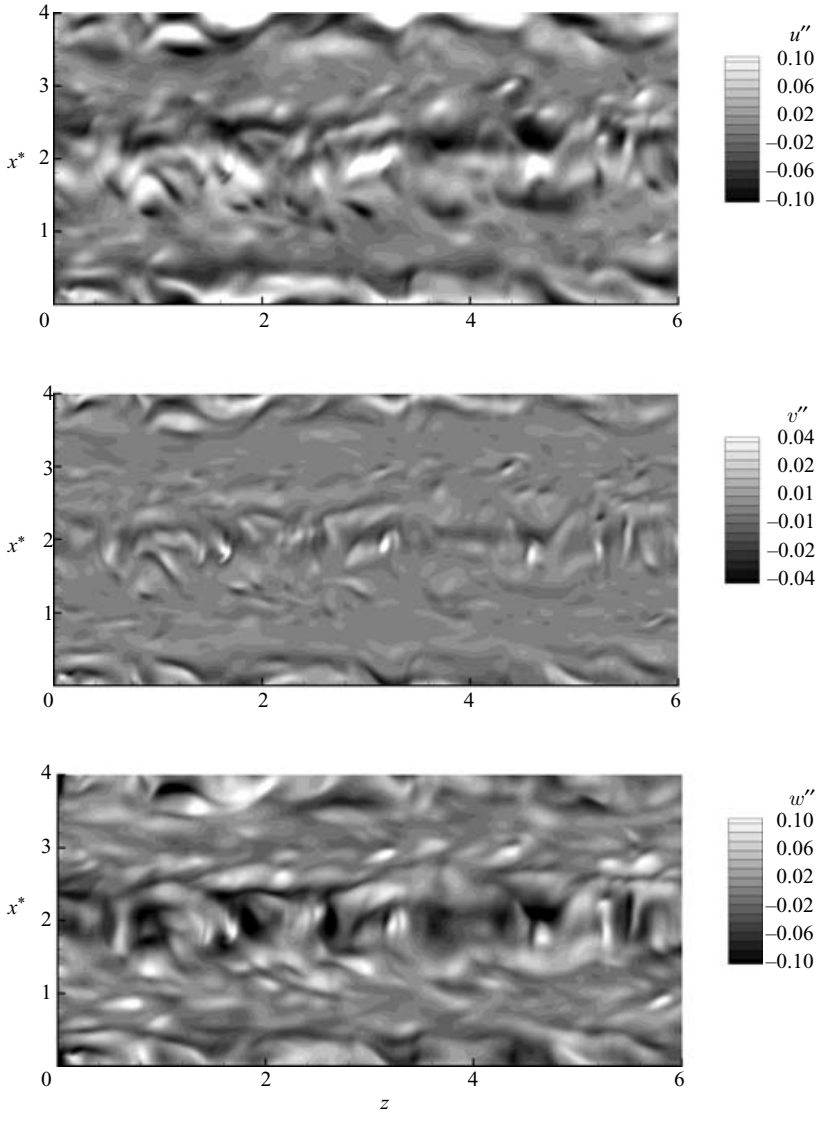

FIGURE 37. Visualization of velocity fluctuations in the x^*–z^* plane at $y_2^+ = 3.87$.

streaks occur in all three velocity components and are limited to an axial location where the vortex motion is away from the inner cylinder. The structure and magnitude of the turbulent velocity fluctuations are clearly influenced by the TV motion, with the largest fluctuation concentrated at the vortex outflows. The location of the streaks can be linked to the near-wall secondary vortex structures observed for the mean velocity field (figure 18).

Near the outer cylinder at $y_2^+ = 3.87$, a streaky structure could not be detected; however, the TV motion is still having an influence as evidenced by the banded structure (figure 37). The apparent lack of a streaky structure is consistent with the very weak vortex structures observed near the outer cylinder in figure 18. A banded structure is also observed at $y_1^+ = 98$ (midway between the cylinders) (figure 38).

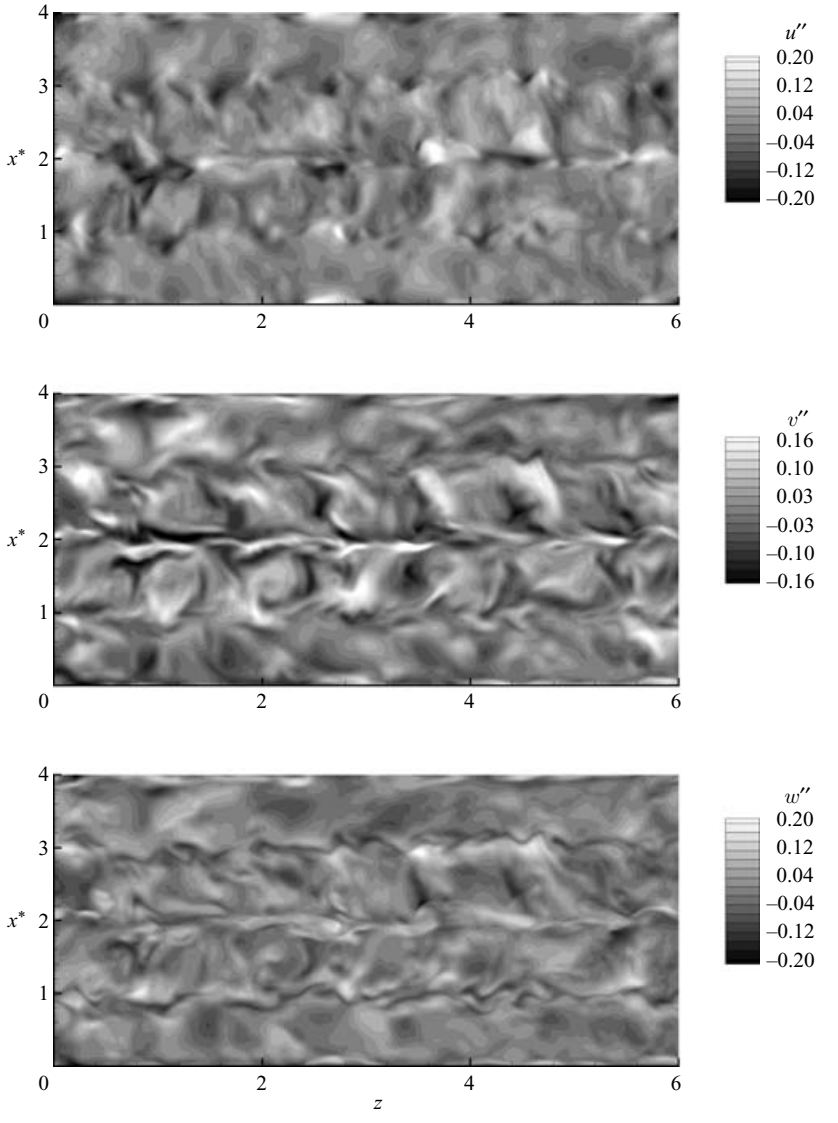

FIGURE 38. Visualization of velocity fluctuations in the x^*–z^* plane at $y_1^+ = 98$.

Very broad bands are observed in v'' and w'' at the TV boundaries. The u'' velocity component shows less evidence of this structure.

In the x^*–r^* plane, the relationship between the instantaneous streamwise velocity field and velocity fluctuations in the plane is of interest. Figure 39 shows vectors of u' and v' on contours of the instantaneous streamwise velocity, and also vectors of u'' and v'' on contours of the instantaneous streamwise velocity. When the TV component is retained (that is, the fluctuations are viewed as u' and v'), there is a similarity between the changes in the streamwise velocity contour and the velocity components perpendicular to the streamwise direction. However, unlike flow in a boundary-layer, channel or pipe, there is no direct visual correlation between the turbulent velocity fluctuations (u'' and v'') and the streamwise velocity. This gives insight into the mechanism of instantaneous momentum transfer between the two cylinders. The TV

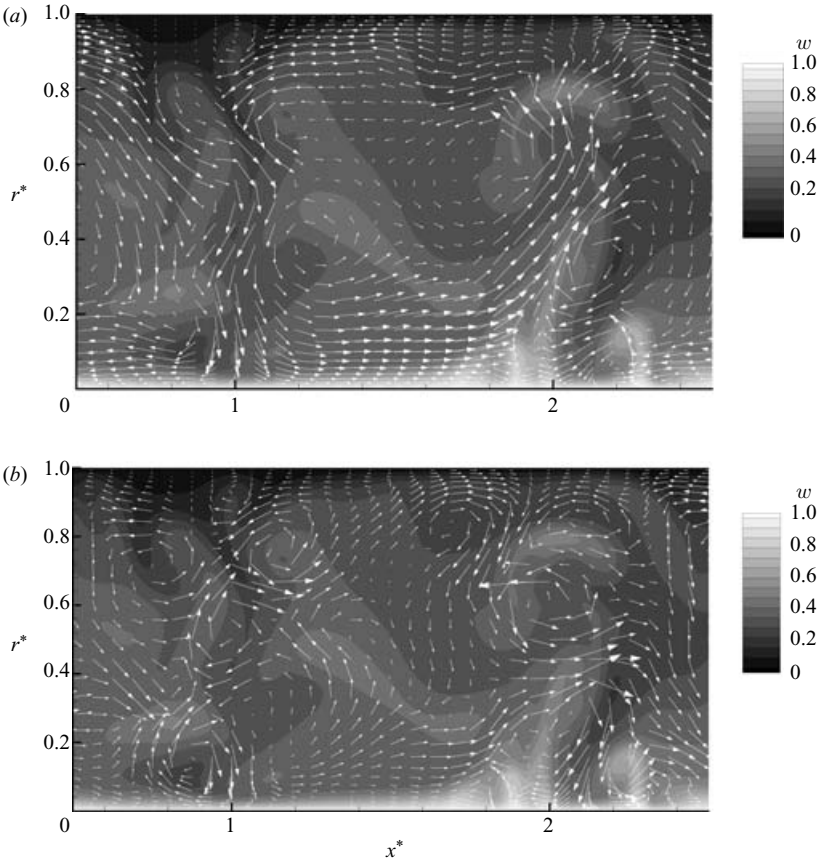

FIGURE 39. (*a*) Vectors of u' and v' on contours of w, (*b*) vectors of u'' and v'' on contours of w.

motion takes a large portion of high-momentum fluid from the inner cylinder at $x^* \approx 2$ and it brings low-momentum fluid in at $x^* \approx 1$. There is a noticeable thickening and thinning of the boundary layer on the inner cylinder associated with this process as well as the existence of a stagnation point near $x^* = 1$ at the inner cylinder.

6. Conclusion

DNS of turbulent TC flow has been carried out for a Reynolds number of 3200 in a device with a radius ratio of 0.617. Results from the simulation have been compared with available experimental data with good agreement of trends. A comprehensive verification exercise was undertaken to ensure the flow state achieved was repeatable and corresponded to the features of turbulent TC flow.

Inspection of the mean velocity field identified a mean motion consisting of TV pairs and secondary vortex pairs confined to the near-wall region at locations where the mean TV motion was directed away from either cylinder. The secondary vortices are seen to cause significant change in the mean wall shear stress, particularly at the vortex inflows and outflows from either cylinder. The mean TV motion was found to make a significant contribution to the velocity fluctuations when results were averaged in the axial direction and the TV motion was included as part of

the velocity fluctuation. This indicated that a large proportion of the momentum transport between the cylinders was localized owing to the mean TV motion. This was confirmed by investigation of the mean and Reynolds shear stress terms over the cylinder gap width.

Reynolds stress budgets, based on the turbulent and TV velocity fluctuations are reported. One of the more significant results to come from this effort was the confirmation that the role of pressure is more complex for turbulent TC flow when compared with plane boundary-layer flow (that is, pipe or channel flow). The pressure terms are usually responsible for a transfer of streamwise velocity fluctuations to the transverse directions. This is still observed, however, in turbulent TC flow, the transfer of streamwise velocity fluctuations is a result of convective (bulk velocity gradient effect) and pressure effects. There is still pressure transfer from the streamwise velocity fluctuation, but it is small compared with other terms. In the wall-normal velocity fluctuation budget, dissipation is minimal and pressure terms actually act to transfer some of the velocity fluctuations. Production of velocity fluctuations occurs through a mean field interaction effect (identified as C_{vv}) rather than as a result of the local gradient of mean velocity. Pressure terms are seen to be the main source of spanwise velocity fluctuations.

Finally, visualization of the turbulent velocity fluctuations was performed. The visualization revealed a streaky structure near the inner cylinder. The structure was confined to locations where the mean TV motion was away from the inner cylinder. Near the outer cylinder, the streaky structure could not be identified; however, the velocity fluctuations still had a banded structure of low- and high-magnitude fluctuation as a result of the mean TV motion. Visualization in a plane perpendicular to the mean flow direction revealed that there was a good correlation between the instantaneous velocity fluctuations and the streamwise velocity magnitude, but only when the velocity fluctuations included fluctuations due to turbulence and the mean TV motion, thus indicating the significant role of the mean TV motion in momentum transport.

Computer time for this work was provided by an Australian Partnership for Advanced Computing grant and the Queensland Parallel and Supercomputing Foundation. M. Bilson was supported by an Australian Postgraduate Award Scholarship.

REFERENCES

Akselvoll, K. & Moin, P. 1996 An efficient method for temporal integration of the Navier–Stokes equation in confined axisymmetric geometries. *J. Comput. Phys.* **125**, 454–463.

Andereck, C. D., Liu, S. S. & Swinney, H. L. 1986 Flow regimes in a circular Couette system with independently rotating cylinders. *J. Fluid Mech.* **164**, 155–183.

Barcilon, A. & Brindley, J. 1984 Organized structures in turbulent Taylor–Couette flow. *J. Fluid Mech.* **143**, 429–449.

Batten, W. M. J., Bressloff, N. W. & Turnock, S. R 2002 Transition from vortex to wall driven turbulence production in the Taylor–Couette system with a rotating inner cylinder. *Intl J. Numer. Meth. Fluids* **38**, 207–226.

Bendat, J. S. & Piersol, A. G. 1971 *Random Data: Analysis and Measurement Procedures*. Wiley-Interscience.

Bilson, M. 2004 Momentum and scalar transport in the straight pipe and rotating cylinder – a comparison of transport mechanisms. PhD thesis, Division of Mechanical Engineering, The University of Queensland.

Bilson, M. & Bremhorst, K. 2003 Comparison of turbulent scalar transport in a pipe and a rotating cyliner. *Intl Conf. on CFD in the Minerals and Process Industries*, pp. 493–498.

Bilson, M. & Bremhorst, K. 2004 DNS study of the instantaneous and mean scalar transport in turbulent Taylor–Couette flow. *11th Intl Symp. on Flow Visualization*, University of Notre Dame, Notre Dame, Indiana, USA, August, pp. 9–12.

Bradshaw, P. 1971 *An Introduction to Turbulence and its Measurement*. Pergamon.

Coles, D. 1965 Transition in circular Couette flow. *J. Fluid Mech.* **21**, 385–425.

DiPrima, R. C. & Swinney, H. L. 1981 *Hydrodynamic Instabilities and the Transition to Turbulence*, chap. 6, p. 139. Springer.

Dukowicz, J. K. & Dvinsky, A. S. 1992 Approximate factorization as a high order splitting for the implicit incompressible flow equations. *J. Comput. Phys.* **102**, 336–347.

Eggels, J. M., Unger, F., Weiss, M. H., Westerweel, J., Adrian, R. J., Friedrich, R. & Nieuwstadt, F. T. M. 1994 Fully developed turbulent pipe flow: a comparision between direct numerical simulation and experiment. *J. Fluid Mech.* **268**, 175–209.

Fenstermacher, P. R., Swinney, H. L. & Gollub, J. P. 1979 Dynamical instabilities and the transition to chaotic Taylor vortex flow. *J. Fluid Mech.* **94**, 103–128.

Ferziger, J. H. & Peric, M. 2002 *Computational Methods for Fluid Dynamics*, 3rd edn. Springer.

Gabe, D. R. 1974 The rotating cylinder electrode. *J. Appl. Electrochem.* **4**, 91–108.

Gabe, D. R. & Walsh, F. C. 1983 The rotating cylinder electrode: a review of development. *J. Appl. Electrochem.* **13**, 3–22.

Gabe, D. R., Wilcox, G. D., Gonzales-Garcia, J. & Walsh, F. C. 1998 The rotating cylindrical electrode: its continued development and application. *J. Appl. Electrochem.* **28**, 759–780.

Gorman, M. & Swinney, H. L. 1982 Spatial and temporal characteristics of modulated waves in the circular Couette system. *J. Fluid Mech.* **117**, 123–142.

Harlow, F. H. & Welch, J. E 1965 Numerical calculation of time-dependent viscous incompressible flow of fluid with free surface. *Phys. Fluids* **8**, 2182–2189.

Haut, B., Ben Amor, H., Coulon, L., Jacquet, A. & Halloin, V. 2003 Hydrodynamics and mass transfer in a Couette–Taylor bioreactor for the culture of animal cells. *Chem. Engng Sci.* **58**, 777–784.

Hockney, R. W. 1965 A fast direct solution of Poisson's equation using Fourier analysis. *J. Assoc. Comput. Machinery* **12**, 95–113.

Hoffman, J. 1982 *J. Comput. Phys.* **46**, 469–474.

Kataoka, K., Doi, H. & Komai, T. 1977 Heat/mass transfer in Taylor vortex flow with constant axial flow rates. *Intl J. Heat Mass Transfer* **20**, 57–63.

Kawamura, H., Ohsaka, K., Abe, H. & Yamamoto, K. 1998 DNS of turbulent heat transfer in channel flow with low to medium-high Prandtl number fluid. *Intl J. Heat Fluid Flow* **19**, 482–491.

Kobayashi, M., Maekawa, H., Takano, T. & Yamada, Y. 1990 An experimental study on turbulent Taylor vortex flow between concentric cylinders. *JSME Intl J.* II **33**, 436–445.

Kobayashi, M., Matsubara, K. & Maekawa, H. 1999 Prediction of the turbulent Taylor vortex flow between concentric rotating cylinders. *Intl J. Transport Phenomena* **1**, 245–254.

Koschmieder, E. L. 1979 Wavelength measurements in turbulent Taylor vortex flow. *J. Fluid Mech.* **93**, 515–527.

Kravchenko, A. G & Moin, P. 1997 On the effect of numerical errors in large-eddy simulations of turbulent flows. *J. Comput. Phys.* **131**, 310–322.

Lathrop, D. P Fineberg, J. & Swinney, H. L. 1992 Turbulent flow between concentric rotating cylinders at large Reynolds number. *Phys. Rev. Lett.* **68**, 1515–1518.

Loulou, P., Moser, R. D., Mansour, N. N. & Cantwell, B. J. 1997 Direct numerical simulation of incompressible pipe flow using a B-spline spectral method. *NASA TM* 110436.

Moin, P. & Mahesh, K. 1998 Direct numerical simulation: a tool in turbulence research. *Annu. Rev. Fluid Mech.* **30**, 539–578.

Moser, R. & Moin, P. 1987 The effects of curvature in wall-bounded turbulent flows. *J. Fluid Mech.* **175**, 479–510.

Parker, J. & Merati, P. 1996 An investigation of turbulent Taylor–Couette flow using laser Doppler velocimetry in a refractive index matched facility. *Trans. ASME* I: *J. Fluids Engng* **118**, 810–818.

Perot, J. B. 1993 An analysis of the fractional step method. *J. Comput. Phys.* **108**, 51–58.

Rudman, M. J. & Blackburn, H. M. 1998 Turbulent Taylor–Couette flow. *13th Australasian Fluid Mech. Conf.* pp. 163–166.

Smith, G. P. & Townsend, A. A. 1982 Turbulent Couette flow between concentric cylinders at large Taylor numbers. *J. Fluid Mech.* **123**, 187–217.

Tafti, D. 1996 Comparison of some upwind-biased high-order formulations with a second-order central-difference schmeme for time integration of the incompressible Navier–Stokes equations. *Comput. Fluids* **25**, 647–665.

Tagg, R. 1994 The Couette–Taylor problem. *Nonlin. Sci. Today* **4**, 2–23.

Takeda, Y. 1999 Quasi-periodic state and transition to turbulence in a rotating Couette system. *J. Fluid Mech.* **389**, 81–99.

Taylor, G. I. 1923 Stability of a viscous fluid contained between two rotating cylinders. *Phil. Trans. R. Soc. Lond.* **223**, 289–343.

Taylor, G. I. 1935 Distribution of velocity and temperature between concentric rotating cylinders. *Proc. R. Soc.* A **151**, 494–512.

Vasilyev, O. V. 2000 High order finite difference schemes on non-uniform meshes with good conservation properties. *J. Comput. Phys.* **157**, 746–761.

Wattendorf, F. L. 1935 A study of the effect of curvature on fully developed turbulent flow. *Proc. R. Soc. Lond.* A **148**, 565–598.

Wendt, F. 1933 *Ingenieur-Archiv.* **4**, 577.

Wereley, S. T. & Lueptow, R. M. 1994 Azimuthal velocity in supercritical circular Couette flow. *Exps. Fluids* **18**, 1–9.

Wilcox, D. 1993 *Turbulence Modelling for CFD*. DCW Industries.

Wild, P. M., Djilali, N. & Vickers, G. W. 1996 Experimental and computational assessment of windage losses in rotating machinery. *Trans. ASME* I: *J. Fluids Engng* **118**, 116–122.

Yuu, S. & Umekage, T. 1995 Direct numerical simulation of three-dimensional Navier–Stokes equations for turbulent circular Couette flows ($Re = 1500$) and experimental verification. *Kagaku Kogaku Ronbunshu* **21** (5), 886–895 (in Japanese).